UNIVERSITY OF CALIFORNIA,
IRVINE

Exploring fundamental physics with small-scale structures

DISSERTATION

submitted in partial satisfaction of the requirements
for the degree of

DOCTOR OF PHILOSOPHY

in Physics and Astronomy

by

Andrew S. Graus

Dissertation Committee:
Professor James S. Bullock, Chair
Associate Professor Michael Cooper
Professor Manoj Kaplinghat

2018

TABLE OF CONTENTS

LIST OF FIGURES

LIST OF TABLES

ACKNOWLEDGMENTS

I would like to thank...

support by an AGEP-GRS supplement to NSF grant AST- 1009973.

Monthly Notices of the Royal Astronomical Society who published the text that appears in Chapters 2 and 3.

Michael Boylan-Kolchin, who helped with the work that appears in Chapters 2, 3 and 4

Daniel Weisz, who helped with the work that appears in Chapters 2 and 4

Anna Nierenberg, who helped with the work that appears in Chapter 3.

CURRICULUM VITAE

Andrew S. Graus

EDUCATION

Doctor of Philosophy in Physics and Astronomy **2018**
University of California, Irvine *Irvine, CA*

Bachelor of Science in Astronomy and Astrophysics **2012**
University of Michigan *Ann Arbor, MI*

RESEARCH EXPERIENCE

Graduate Research Assistant **2014–2018**
University of California, Irvine *Irvine, CA*

Undergraduate Researcher **2009–2012**
University of Michigan *Ann Arbor, MI*

TEACHING EXPERIENCE

Teaching Assistant **2012–2014**
University of California, Irvine *Irvine, CA*

ABSTRACT OF THE DISSERTATION

Exploring fundamental physics with small-scale structures

By

Andrew S. Graus

Doctor of Philosophy in Physics and Astronomy

University of California, Irvine, 2018

Professor James S. Bullock, Chair

One of the goals of theoretical galaxy formation is to use simulations combined with observations in order to constrain the fundamental physics that govern the formation of galaxies. Of particular interest are physical processes that can impact the formation of small-scale structures. Among the things we can potentially constrain with a combination of observations and simulations of small-scale structures are stellar feedback, reionization, and dark matter particle physics. We investigate several promising avenues to constrain fundamental physics with simulations of galaxy formation. First, we use the star formation histories (SFH) for Local Group dwarf galaxies in order to constrain high-redshift stellar mass functions (SMFs). Second, we look at the destruction of substructure around large galaxies, and how it may impact the detection of substructure via subhalo lensing. Finally, we use full hydrodynamics simulations of Local Volume dwarf galaxies in order to investigate the impact of stellar feedback on the age distributions of stars within these galaxies.

Chapter 1

Introduction

A key technique in theoretical galaxy formation is to take models and simulations of galaxies, and predict what they would imply for observed properties of galaxies. These can then be compared to the actual universe to understand what processes dominate the formation of galaxies. Such studies have seen success on large scales ($\geq$ 10 Mpc) where the distribution of galaxies in simulated volumes matches the observed distribution (e.g. Springel et al., 2006). However, similar experiments on smaller scales, such as the satellite galaxies of the Milky Way and Andromeda, have unveiled a number of issues that are currently the subject of much investigation (Bullock & Boylan-Kolchin, 2017). Such small structures represent the limits of galaxy formation, and thus are impacted by changes several changes to fundamental physics including the impact of stellar feedback (such as supernovae or radiative feedback), when reionization occurred, and dark matter particle physics.

Supernova feedback can impact the formation of galaxies in a few ways. It has been shown to create cores in the dark matter halo profiles (Pontzen & Governato, 2012; Oñorbe et al., 2015; Fitts et al., 2017). It also could potential play a key role in the creation of age and metallicity gradients in the stellar distributions of dwarf galaxies (El-Badry et al., 2016).

The impact of feedback is strong in dwarf galaxies because they have large stellar masses compared to their dark matter halo masses, meaning that they are more likely to be impacted by strong feedback from stars.

Furthermore, different theories of dark matter can have an impact on small structures. These theories are motivated, in part, by constraints of dark matter that come from large-scale structure. These constraints tell us that the dark matter particle must act similar to a standard Cold Dark Matter (CDM) Weakly-interacting massive particle (WIMP) at large scales. However, there are several valid theories of dark matter that can reproduce large-scale structure seen in CDM, but predict different properties for small-scale structures. For example, self-interacting dark matter, in which the dark matter particle has a non-zero scattering cross-section with itself. This creates additional heating when dark matter halo densities are high, such as at the cores of dwarf galaxies. This additional interaction can create cores in a manner similar to what is expected from supernovae (Elbert et al., 2015). A second alternative theory of dark matter is warm dark matter (WDM), where the dark matter particle is less massive than a typical WIMP. This "hotter" dark matter washes out perturbations on small-scales, meaning small dark matter halos will fail to form. Fewer small halos would imply fewer small galaxies that we could observe around the Milky Way, potentially allowing us to constrain dark matter theories (Polisensky & Ricotti, 2011).

Similarly, the number of galaxies we can see is strongly dependent on reionization. Reionization is the process by which neutral hydrogen was ionized in the early universe. Once the Cosmic Microwave Background (CMB) formed, the gas in between galaxies became neutral. However, in the present-day universe this gas is ionized, implying some process must have reionized this gas. It is believed that this was caused by the formation of the first stars and galaxies, which produce high energy UV photons, and can ionize Hydrogen (Alvarez et al., 2012; Kuhlen & Faucher-Giguère, 2012; Schultz et al., 2014; Robertson et al., 2015; Bouwens et al., 2015). However, it is also possible that this ionizing radiation could impact the star

formation in very small dark matter halos either shutting down their star formation early on, or even preventing it entirely (Efstathiou, 1992a; Bullock et al., 2000). An interesting uncertainty in this process is when exactly reionization occurred. Current evidence from the Planck satellite suggests that reionization occurred sometime between $z = 7.9$ and 9.7 (Planck Collaboration et al., 2016). However, the timing of reionization could potentially have a large impact on the galaxy distribution.

This clearly highlights how different physical processes that can impact small dark matter halos, and the galaxies that form in them. One key issue is that many of these processes can impact the distributions of halos and galaxies in similar ways. Both supernovae feedback, and self-interacting dark matter can create cored dark matter halo profiles. Both WDM, and reionization can reduce the total number of small galaxies. While the effects of these different processes can be qualitatively similar it could be possible to decouple the effect of these different models in the near future. The purpose of this work is to investigate several different methods by which we could potentially decouple the impact of different physics on the population of small galaxies, and constrain models of feedback, dark matter, and the timing of reionization. Chapter 2 will focus on using the archaeological record of star formation in Local Group dwarf galaxies to constrain the stellar mass function. Chapter 3 will focus on the field of substructure lensing which could allow us to see small dark matter halos that fail to form galaxies, and place constraints on both reionization and alternative dark matter theories. Finally Chapter 4 will look in-depth at cosmological simulations of dwarf galaxies in order to investigate the observable impact of stellar feedback in these systems.

1.1 Measuring stellar mass functions

The Stellar Mass Function (SMF) is simply a measure of the density of galaxies as a function of their stellar mass, and is often parameterized by a Schechter function:

$$\phi(M_\star)dM_\star = (\phi^\star/M^\star) \times (M_\star/M^\star)^\alpha \exp[-(\mathrm{M}_\star/\mathrm{M}^\star)]\mathrm{dM}_\star$$

Where ϕ is the number density of galaxies per volume (often Mpc^{-3}) and $M_\star$ is the stellar mass of the galaxy. The rest of the variables are all parameters that are fit which determine the characteristic shape of the Schechter function (an exponential function with a power-law cutoff). $M^\star$ determines the location of the cutoff, α determines the power law slope after the cutoff, and $\phi^\star$ is an overall normalization of the density.

Constraining the stellar mass function is important as we can use it to get a statistical measure of the number of galaxies in the universe. This can then be compared to models, including cosmological simulations, to bet a better sense of the physical processes that dominate the formation of galaxies. Of particular importance to this work is the low-mass or faint-end of the luminosity function. If we can constrain the stellar mass function at low masses ($M_{star} \leq 10^6\ M_\odot$) theory speculates that we may see a deviation from a power law or even a complete cutoff due to reionization or potentially different dark matter theories. One of the difficulties of measuring the stellar mass function at high redshift is that those galaxies are incredibly faint, and currently the speculated region where we could see a cutoff lies just out of reach of current technology.

In Chapter 2 we look at an alternative method for constraining the high redshift stellar mass function at low masses, which relies on Local Group star formation histories. We can use the archaeological record of star formation in Local Group galaxies to get a sense of what the low-mass galaxy population looks like at high redshift. We can then estimate the stellar

mass function by using simulated Local Groups to constrain the volume that these galaxies occupy, and place constraints on the stellar mass function.

1.2 Probing fundamental physics with substructure lensing

The second technique we focus on in Chapter 3 is that of substructure lensing. One of the issues with constraining dark matter using astrophysics is that we often have to rely on studying galaxies. This can lead to confusion in how to relate the observed galaxy to its underlying dark matter distribution, contaminating any potential signals from dark matter. However, theory suggests there is a mass scale below which dark matter halos won't form a galaxy due to reionization (Bullock et al., 2000; Sawala et al., 2016b). If we can detect these galaxy-less dark matter halos we could potentially study dark matter. For example, CDM predicts that there should be dark matter halos down to low masses, however, WDM predicts a cutoff at halo masses of about 10^8 $M_\odot$. One promising way to detect these dark halos is via gravitational lensing. Gravitational lensing occurs when light from a distant system encounters a massive object on its path, the massive object bends the light creating distortions. These distortions depend on the mass of the object encountered and the distribution of that mass. Therefore, these distortions can be modeled and used to measure the total mass of objects in the universe (including dark matter).

Gravitational lensing systems are often modeled as smooth halos, however, in the real universe these systems will have substructure which could perturb the lensing system. One way we could detect substructure is by looking at a gravitational lensing system modeling the system as a smooth lens and then comparing it to the residual with the true data. This technique has already seen some success in detecting substructure (Vegetti et al., 2012;

Hezaveh et al., 2016), and will continue to expand in the near future as many more lensing systems will be found (Collett, 2015). However, this field is still quite young, and the theoretical expectations for CDM are still unknown. In particular, recent theoretical results have suggested that full hydrodynamics simulations of large galaxies can destroy additional substructure (Garrison-Kimmel et al., 2017; Zhu et al., 2016; Despali & Vegetti, 2016; Chua et al., 2016). This could potentially have a massive impact on predictions from substructure lensing. Chapter 3 will focus on the Illustris-1 and Illustris-1 dark simulations (Nelson et al., 2015; Vogelsberger et al., 2014a) which we have used to make predictions for substructure lensing and compare and contrast the substructure populations of potential lensing systems.

1.3 Studying the impact of feedback on stellar populations with dwarf galaxy simulations

In Chapter 4 we study the impact of stellar feedback on small-scale structures. Stellar feedback has been invoked to solve numerous issues with small-scale structures. For example, the cusp-core problem (Flores & Primack, 1994) where observed dwarf galaxies sometimes appear to have cored dark matter halo profiles, however CDM halos are characterized by a more dense dark matter cusp. Supernova feedback has also been invoked in solving the "Too Big To Fail" problem (Boylan-Kolchin et al., 2011) where the most dense subhalos of the Milky Way are too dense to host the most massive galaxies. Recent simulations incorporating more sophisticated models of supernova and radiation pressure feedback have gone a long way toward resolving these problems (Wetzel et al., 2016; Sawala et al., 2016c; Oñorbe et al., 2015; Fitts et al., 2017), however some lingering questions remain. While supernova feedback can solve these problems it is still unclear how strong the feedback must be in order to solve these issues, but still create realistic galaxies.

Chapter 4 will focus on one method by which we could potentially constrain models of feedback by looking at the stellar distributions within dwarf galaxies. Within simulations star particles are modeled as collisionless, similar to dark matter. Because of this the star particles should be subject to the same physical processes as seen in the dark matter distributions. The dark matter particles can be heated over time by supernova feedback, and therefore it is reasonable to assume that the same is true for the star particles. Star particles in these simulations are also subject to an additional form of heating. Explosive feedback events can drive gas outflows, this additional pressure can possibly trigger star formation leading forming stars with very large radial velocities. In Chapter 4 we investigate this process in depth by looking at dwarf galaxy simulations run with the GIZMO code (Hopkins, 2015) and FIRE-2 feedback implementation (Hopkins et al., 2017). These galaxies illustrate the impact of feedback on the stellar distributions of the galaxies, and could potentially be useful in constraining models of feedback.

Chapter 2

Near-field cosmology with dwarf galaxy star formation histories

2.1 Introduction

The evolution of the galaxy stellar mass function, from high-redshift to low, provides an important benchmark for self-consistent galaxy formation models set within the Lambda Cold Dark Matter (ΛCDM) framework (White & Rees, 1978; Somerville & Davé, 2015; Vogelsberger et al., 2014b; Schaye et al., 2015a). In particular, the low-mass slope of the stellar mass function (hereafter, $\alpha_{\rm faint}$) is a crucial gauge of how and when feedback becomes important in suppressing galaxy formation in small dark matter halos. Indeed, many of the best models today predict that the galaxy stellar mass function should be much steeper at high redshift than low redshift, more faithfully tracing the dark matter halo mass function slope itself (e.g., Genel et al., 2014; Furlong et al., 2015), while others produce a flatter slope at high redshifts via strong feedback (Lu et al., 2014). As we detail below, a survey of the observational literature over the last several years finds little agreement on whether the

stellar mass function was much steeper at $z = 2 - 5$ than it is at $z = 0$. In what follows, we use local observations to inform this question, relying on the large, uniform sample of star formation histories (SFHs) that are now available for local dwarf satellite galaxies (Weisz et al., 2014a) together with the `ELVIS` N-body simulation suite of the Local Group (Garrison-Kimmel et al., 2014) to connect local galaxy properties to the global galaxy population over cosmic time.

Significant effort has been dedicated to characterizing the galactic stellar mass function (GSMF) and its evolution. A good $z \sim 0$ reference point comes from Baldry et al. (2012), who have used data from the GAMA survey to characterize the GSMF down to $M_\star = 10^8 M_\odot$ and find $\alpha_{\rm faint} \simeq -1.47$. This result has been echoed by other recent work such as Moustakas et al. (2013) whose result agrees quite well with the Baldry et al. (2012) stellar mass function, although they do not quote a value for $\alpha_{\rm faint}$.

Characterizing the mass function at higher redshift is also a priority. However, the results have been divergent, despite a significant effort. For example, Pérez-González et al. (2008) and Marchesini et al. (2009) both reported fairly flat slopes with $\alpha_{\rm faint} \simeq -1$ to -1.2 out beyond $z = 2$, while González et al. (2011) found steeper low-mass slopes $\alpha_{\rm faint} \simeq -1.4$ to -1.6 from redshift $z = 4 - 6$, consistent with little evolution from the $z \sim 0$ value. Still a different conclusion was presented by Santini et al. (2012), who reported significant evolution, with a slope similar to the low-redshift value $\alpha_{\rm faint} \simeq -1.45$ at $z = 1$ but steepening to $\alpha_{\rm faint} \simeq -1.85$ at $z = 3$.

Recent work has explored the stellar mass function to lower stellar masses, but there is still no consensus on the value of $\alpha_{\rm faint}$ and its evolution. Ilbert et al. (2013) report best-fit slopes $\alpha_{\rm faint} \simeq -1.45$ to -1.6 out to $z \simeq 1.5$ using UltraVISTA and Tomczak et al. (2014) use ZFOURGE/CANDELS and find similar best-fit values of $\alpha_{\rm faint} \simeq -1.5$ to -1.6 out to $z \simeq 3$ with no obvious evolution. In contrast to this apparent lack of evolution, Duncan et al. (2014) have used CANDELS and *Spitzer* IRAC data in the GOODS-S field to quantify the

GSMF and find quite steep slopes ($\alpha_{\rm faint} \simeq -1.75$ to -1.9) at $z = 4 - 5$. Grazian et al. (2015) have done similar work in the CANDELS/UDS, GOODS-South, and HUDF fields and prefer slightly shallower values ($\alpha_{\rm faint} \simeq -1.63$) over the same redshift range. Most recently, Song et al. (2016) have combined the CANDELS (GOODS-N and S) and HUDF fields with the deepest IRAC data to date to characterize the GSMF to an unprecedented depth of $M_\star \simeq 10^7\ M_\odot$ and report an even flatter slope at $z = 4$, $\alpha_{\rm faint} = -1.53$, but see continued steepening to $\alpha_{\rm faint} = -2.05$ at $z = 7$.

The idea that the stellar mass function might be getting steeper at early times is qualitatively consistent with the prevailing notion that cosmic reionization relies fundamentally on ionizing photons produced by a large number of faint galaxies (Alvarez et al., 2012; Kuhlen & Faucher-Giguère, 2012; Schultz et al., 2014; Robertson et al., 2015; Bouwens et al., 2015). Of course, a high comoving abundance of faint galaxies at early times requires that small dark matter halos are efficient at producing stars at this time (e.g., Madau et al., 2014), an idea that is qualitatively at odds with what must happen in the $z = 0$ universe. Specifically, if ΛCDM is correct, then the Milky Way should be surrounded by thousands of small dark matter subhalos ($M_{\rm v} \sim 10^9 M_\odot$), far more than the number observed as dwarf galaxies (Moore et al., 1999; Klypin et al., 1999). Solving the missing satellites problem requires the suppression of galaxy formation in small halos today. When (and if) small dark matter halos transition from being the sites of efficient star formation to less efficient star formation is a question that informs our ideas about the origin of strong feedback in small halos (Jaacks et al., 2013; Wise et al., 2014). Unfortunately, the luminosities of interest are unobservably faint ($M_{\rm UV} \sim -14$ at $z > 6$) with current telescopes, and likely will remain unobservable even in the era of *JWST*.

An alternative way to investigate this question observationally is to use local observations as a time machine (Weisz et al., 2014b; Boylan-Kolchin et al., 2014, 2015), a possibility that is enabled by SFHs derived by deep color-magnitude diagrams from *HST* (Weisz et al., 2014a).

These precise SFHs can be used to calculate UV luminosities for each galaxy at specific redshifts (Weisz et al., 2014b), and demonstrate that the progenitors of many Milky Way's satellites (e.g., Fornax, Sculptor, Draco) had UV luminosities during the epoch of reionization that coincide well with the galaxies that seem to be required to maintain reionization at $z \sim 8$ (Boylan-Kolchin et al., 2015, B15 hereafer). Moreover, by enumerating these galaxies today, and tracking back their expected abundances using N-body simulations, Boylan-Kolchin et al. (2014, B14 hereafter) showed that the $z = 8$ UV luminosity function (LF) must break to a shallower slope than the observed $\alpha \approx -2$ for galaxies fainter than $M_{\rm UV} \sim -14$. The constraint was derived from the seemingly unavoidable prediction that there are hundreds of $z = 0$ surviving descendants of reionization-era atomic cooling halos in the Local Group.

This paper adopts a similar approach as in B14, but now applied to constrain stellar mass functions at intermediate redshfits $z = 2 - 5$. The upper limit of this redshift range is set by the age for reliable SFHs that can be achieved by isochrone fitting, which allows one to measure stellar mass older than ~ 12.5 Gyr (corresponding to $z \sim 5$) but with no finer precision (e.g., Weisz et al., 2014a). The lower limit ($z = 2$) is informed by our theoretical methodology. Specifically, our method relies on studying the high-redshift progenitors of surviving subhalos in the simulations. We associate surviving subhalos with dwarf satellite galaxies and treat their progenitors as typical field galaxies at earlier times. In order to do this, we need to ensure that these systems were not satellites at the redshift of concern. Most subhalos of Milky Way size hosts in our simulations are accreted after $z = 2$ (see Section 2.1 below). After this time, at redshifts $z \lesssim 2$, the SFHs of satellite galaxies are likely affected by environmental quenching (Fillingham et al., 2015; Wetzel et al., 2015b; Rocha et al., 2012), and therefore are poor proxies for typical galaxies in the universe prior to this epoch. By restricting our analysis to $z \geq 2$ we avoid this clear bias.

The paper is organized as follows, Section 2 gives a summary of the simulations and observational data used. Section 3 presents in detail how we used the data to look for the effects

of galaxy suppression at high redshift and presents the main results of this paper. Section 4 discusses the implications of this work, and provides predictions for high redshift stellar mass functions. The conclusions are presented in section 5, along with possible caveats and alternative explanations. The cosmology of the ELVIS suite and thus adopted for the analysis within this paper is WMAP-7 (Larson et al. 2011: σ_8=0.801, $\Omega_m = 0.266$, $\Omega_\Lambda = 0.734$, $n_s = 0.963$, and $h = 0.7$)

2.2 Data

2.2.1 Simulation Data

We make use of the ELVIS suite (Garrison-Kimmel et al., 2014) of N-body simulations, which is composed of 12 pairs of Milky Way-Andromeda analogs along with 24 mass-matched isolated systems for comparison. We use the 10 best-matched Milky Way-Andromeda analogs in this work (see Garrison-Kimmel et al. 2014 for details). The simulations are complete to peak halo masses of $M_{\rm halo} = 6 \times 10^7\ M_\odot$, well below the mass range that can host known (classical) satellite galaxies of the Milky Way (e.g. Boylan-Kolchin et al., 2012), which are the points of comparison in this paper. Crucial to our analysis is the ability to connect bound subhalos at $z = 0$ to their progenitors at higher redshift. We do this using the merger trees provided in the public ELVIS data base[1], which were constructed using the Rockstar (Behroozi et al., 2013b) halo finder.

For our high redshift analysis we use only subhalos that survive as bound substructures at $z = 0$ within 300 kpc of either host. We make no assumption as to which of the pairs on the ELVIS catalogs would be the Milky Way or Andromeda. This assumption is fair because the mass estimates of the Milky Way and Andromeda are the same within errors (van der

[1] http://localgroup.ps.uci.edu/elvis/

Marel et al. 2012; Boylan-Kolchin et al. 2013).

One of our main assumptions in this work is that it is fair to treat the main progenitors of subhalos as typical galaxies prior to the time they first became subhalos. We know that classical dwarf satellite galaxies are more likely to be quenched than their counterparts in the field (Mateo, 1998) and we therefore want to avoid this bias in our analysis. [2]

Using the ELVIS simulations, Wetzel et al. (2015a) found that $\sim 84\%$ of subhalos in the relevant mass range were accreted after $z = 2$ and $\sim 98\%$ were accreted after $z = 3$. Our own independent analysis yields similar results (see also Fillingham et al., 2015). This fact motivates our use of $z = 2$ as the lower bound on the redshift range. We note that this choice is also consistent with direct estimates for the accretion times of the classical Milky Way satellites from Rocha et al. (2012), who find that only one of the Milky Way satellites in our sample (Ursa Minor) is consistent with having been accreted before $z = 2$, with an infall time between 8 and 11 Gyr ago.

2.2.2 Observational Data

Milky Way Satellite Star Formation Histories

The star SFHs of Milky Way satellites are taken from the data sets of (Weisz et al., 2014a, W14) and Weisz et al. (2013, W13), which rely color magnitude diagrams from archival *HST*/WFPC2 observations. We refer the reader to Weisz et al. (2014a) and Dolphin (2002) for an in-depth discussion of the techniques used. In what follows we assume that the SFHs are applicable to the entire galaxy, even though in many cases the CMDs were derived from fields that do not cover the entire galaxy. Instead, we use the normalized SFHs from W14 and W13 to the $z = 0$ stellar mass of each Milky Way satellite using the values given in

[2] Ultrafaint galaxies may likely be quenched, even in the field, owing to reionization (Bullock et al., 2000; Ricotti & Gnedin, 2005).

McConnachie (2012), which were calculated based on integrated light, and assuming a mass to light ratio of one.

One of our major concerns is that our comparison set be complete. For this reason, we restrict ourselves to the 12 dwarfs currently within 300 kpc of the Milky Way and with $M_\star^{z=0} > 2{\times}10^5\,M_\odot$: Carina, Canes Venatici I, Draco, Fornax, Leo I, Leo II, LMC, Sagittarius, Sculptor, Sextans, SMC, and Ursa Minor. The SFHs in the W13/W14 data set include all of these bright Milky Way satellites except Sextans. In our fiducial analysis we include Sextans ($M_\star^{z=0} = 4.4 \times 10^5\ M_\odot$) by assuming its normalized SFH is the same as that of Carina ($M_\star^{z=0} = 3.8 \times 10^5\ M_\odot$). We find that alternative choices for Sextans do not strongly alter our results.

High redshift stellar mass functions

We will focus our comparisons to measurements of high-redshift GSMF presented over the last two years. For our $z = 2 - 3$ constraints we will normalize at the high-mass end to the results of Ilbert et al. (2013, I13 herafter), who have used UltraVISTA to measure the GSMF to $M_\star \gtrsim 10^{10}\ M_\odot$; and also to those of Tomczak et al. (2014, T14 hereafter), who have pushed a factor of ~ 2 deeper at the relevant redshifts using ZFOURGE/CANDELS.

At $z = 4 - 5$, we will use the *HST*-CANDELS + *Spitzer*/IRAC results from Duncan et al. (2014, D14 hereafter) and the more recent (deeper) study from Song et al. (2016, S15 hereafter), who reach $M_\star \simeq 10^7\ M_\odot$ (vs. $10^8\ M_\odot$ for D14) at these redshifts. Grazian et al. (2015) have presented a similar analysis and their fits are intermediate between those of D14 and S15; we focus on the latter two in our comparison in order to bracket the most recent results.

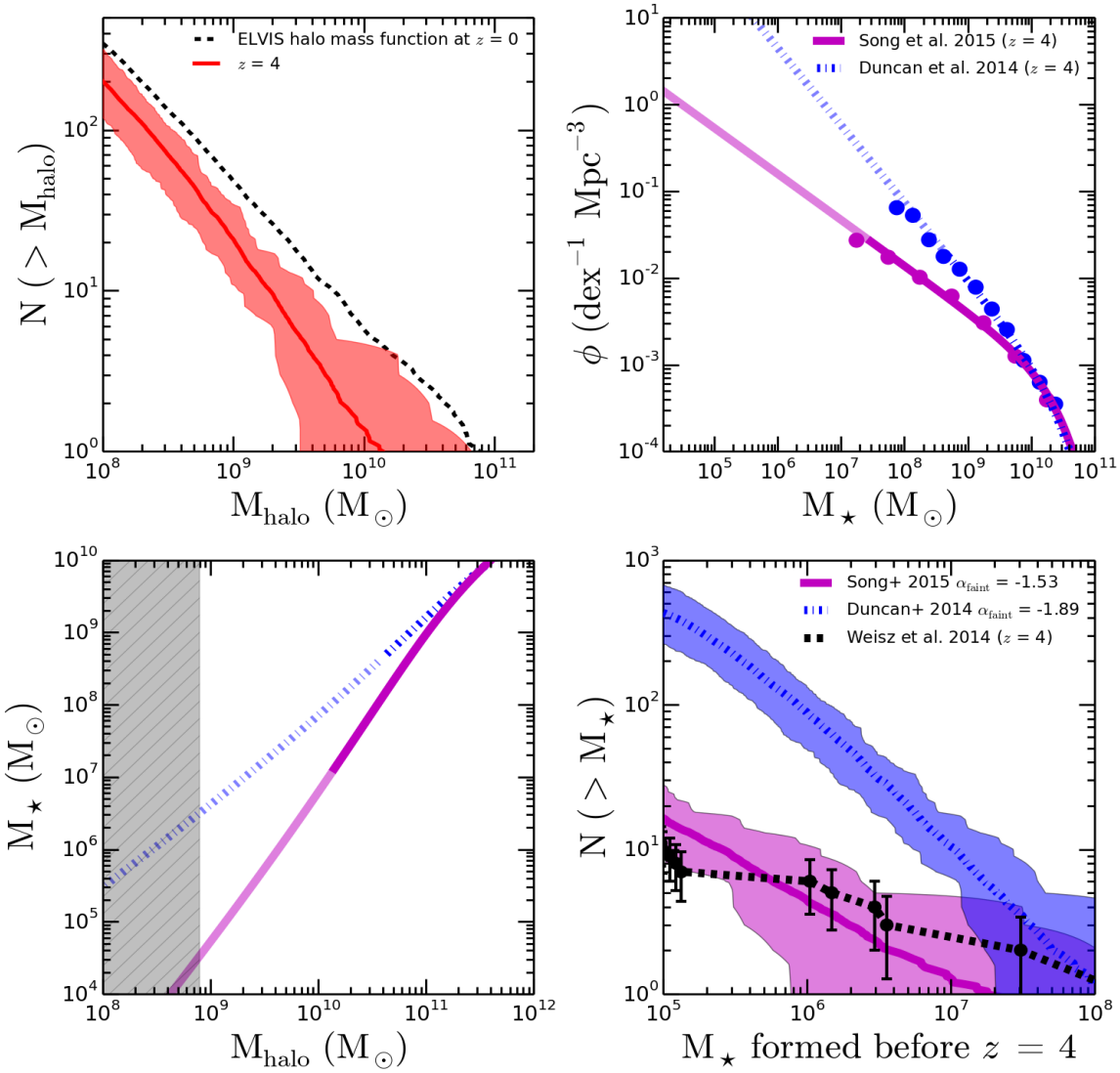

Figure 2.1: *Top left:* Cumulative halo mass functions for all bound objects within 300 kpc of simulated Milky Way analogs from ELVIS. The black dashed line shows the average mass function at $z = 0$. The red line shows the average mass function for main branch halos at $z = 4$ that survive as independent halos to the present day. The shaded band corresponds to the full scatter over all 20 systems. *Top right*: GSMFs from D14 and S14, along with their published Schechter fits extrapolated down to the stellar masses of relevance for this paper. *Bottom left*: The stellar mass vs. halo mass relations that result from the same pair of GSMFs at $z = 4$. The shaded grey band in the lower left panel corresponds to the halo mass scale where galaxy formation may be suppressed by the UV background (Okamoto et al., 2008). *Bottom right*: The implied cumulative stellar mass functions before $z = 4$ that result from combining the upper left and bottom left panels. The data points are measurements for Milky Way satellites from W13 and W14 with Poisson error bars.

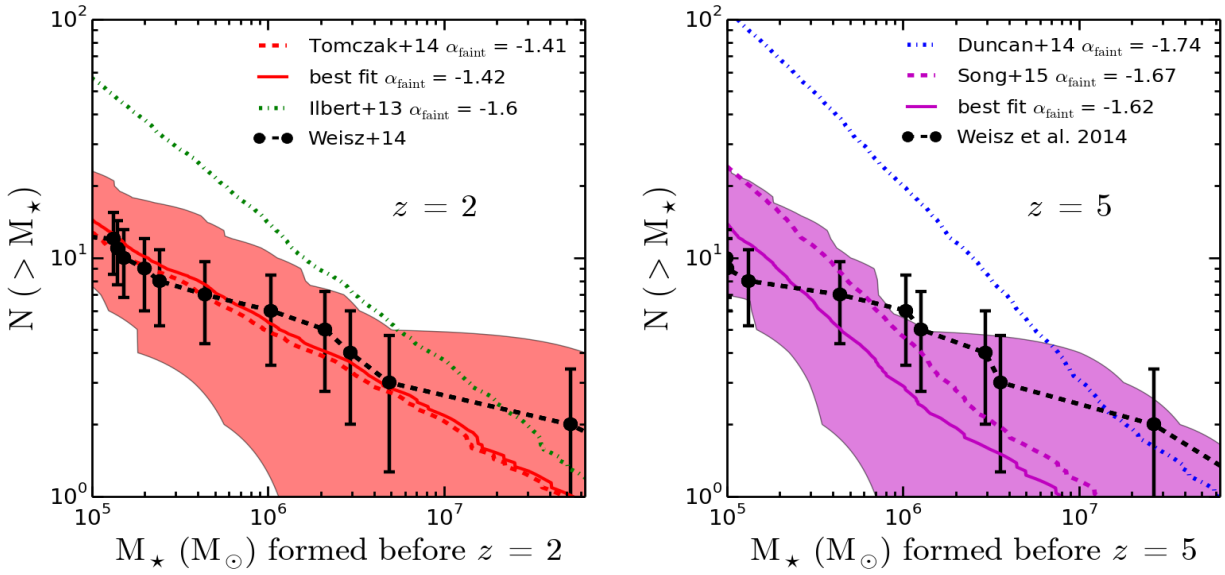

Figure 2.2: Projections of the stellar mass function at low masses from $z = 2$ to $z = 5$ plotted along with present day measurements of the stellar mass function from various sources. The solid lines are best fit faint end slopes derived by fixing the other Schechter parameters to literature values and performing a chi-squared minimization. In general the best fit faint end slope does not differ much from those in the literature, and the faint end slope appears to be consistently near -1.5 for our redshift range.

2.3 Motivation and Methodology

The upper right panel of Figure 1 compares the best-fit GSMFs of D14 (with $\alpha_{\rm faint} = -1.89$) and S15 (with $\alpha_{\rm faint} = -1.53$) at $z = 4$. Table 1 lists the preferred Schechter parameters from D14 and S15; the lines in Figure 1 show these fits and become transparent beyond the last published data point.

Note that the comoving number density of $M_\star = 10^5\ M_\odot$ galaxies in the D14 extrapolation exceeds 10 Mpc^{-3}. Only halos with virial masses below $10^8\ M_\odot$ at these epochs have number densities this high (e.g., Lukić et al., 2007). That is, the only way to have a galaxy population this abundant at $z = 4$ is to associate them with halos of mass $\leq 10^8\ M_\odot$. This becomes problematic when a comparison is made to abundances within the Local Group

The reason this is problematic is implied by the mass functions of the halos in the ELVIS

suite shown in the upper-left panel of Figure 1. The black dashed line shows the average mass function of bound halos within 300 kpc of the ELVIS hosts at $z = 0$ (hereafter called subhalos). The red line shows the mass function of each bound subhalo's *main progenitor* at $z = 4$. The shaded region shows the full scatter in progenitor mass functions over all 20 ELVIS hosts. We see that each Milky Way host should have ~ 200 bound halos within 300 kpc that had progenitors more massive than 10^8 $M_\odot$ at $z = 4$. Given that the number of satellite galaxies of the Milky Way with $M_\star \gtrsim 10^5$ $M_\odot$ is significantly lower than this (12), we know that any GSMF that requires 10^8 $M_\odot$ halos to host $M_\star \gtrsim 10^5$ $M_\odot$ galaxies at $z = 4$ would be inconsistent with known properties of the Milky Way. The aim of this work is to use this basic tension to inform our understanding of the on the low-mass end of the GSMF at high redshifts, place limits on the asymptotic slope $\alpha_{\rm faint}$.

To add some precision to this constraint we rely on abundance matching, and specifically assume that there is a one-to-one relationship between the most massive halos and the most massive galaxies at $z = 4$ (we discuss potential caveats with this assumption in §5). The lower-left panel of Figure 1 shows the implied halo mass / stellar mass relation for both GSMFs. We have used the Sheth et al. (2001) mass function for halo abundances here [3]. These relations allow us to assign a stellar mass to each progenitor subhalo mass at $z = 4$ and then to construct a prediction for satellite stellar mass functions restricted to stars formed before $z = 4$.

The culmination of this exercise is shown in the bottom right panel of Figure 1. The black points show the cumulative function of galaxies within 300 kpc of the Milky Way as a function of $M_\star^{z=4}$ – their mass in ancient stars formed prior to $z = 4$ (from W13, W14). We note that the overall count is low (10 with $M_\star^{z=4} > 10^5$ $M_\odot$) and that the mass function is fairly flat $N \propto (M_\star^{z=4})^{1/3}$. These counts are in stark contrast to what would be expected if an extrapolation of the D14 GSMF were to hold at $z = 4$ (blue), as this would give a

[3] and rely on the hmf Python package (Murray et al., 2013).

steeply rising mass function ($N \propto M_\star^{z=4}$) and result in > 400 galaxies with $M_\star^{z=4} > 10^5$ $M_\odot$. The shading corresponds to the full halo-to-halo scatter in our simulations and the solid line shows the median. If instead we assume the S15 fit holds (magenta), the result is much more in line with the Milky Way data. Another possibility (not shown) is that the D14 normalization is correct but that the stellar mass function at $z = 4$ sharply breaks at $M_\star < 10^7$ $M_\odot$ so that the number density at $M_\star \sim 10^5$ $M_\odot$ is something closer to the S15 extrapolation in the upper right panel.

2.4 Constraints

Figure 2 presents the results of a similar exercise to that performed in the previous section but now at $z = 2$ (left) and $z = 5$ (right). As in the lower right panel of Figure 1, the black points show the cumulative stellar mass functions for Milky Way satellites within 300 kpc, specifically the stellar mass formed prior to $z = 2$ (left, $M_\star^{z=2}$) and $z = 5$ (right, $M_\star^{z=5}$).

The dashed lines in the left panel of Figure 2 shows the implied (median) cumulative mass function, $N(> M_\star^{z=2})$, for the fiducial GSMF at $z = 2$ from I13 (green dash) and T15 (red dash). Note that neither of these data sets were able to reach down to the low stellar masses shown in the plot; the results presented correspond to extrapolations of their double-Schechter fits (with parameters listed in Table 1). Note that I13, motivated by their fits at lower redshift, have fixed $\alpha_{\rm faint} = -1.6$ in their fiducial GSMFs. If this were to hold true, the left-hand side of Figure 2 shows that this would predict typically ~ 55 galaxies within 300 kpc of the Milky Way with more than 10^5 $M_\odot$ in stars older than about 10.4 Gyr ($z = 2$ formation). This is about a factor of five more than observed, which is larger than the halo-to-halo scatter expected from the `ELVIS` suite (shaded red band, see below). The T14 line, on the other hand, agrees fairly well with the Milky Way data, owing primarily to its flatter slope, $\alpha_{\rm faint} = -1.41$.

Table 2.1: Schechter parameters for the reference stellar mass functions used in this work, along with the calculated best fit faint end slopes using local group data. Literature stellar mass functions from Ilbert+ 13 and Tomczak+ 14 were fit using a double Schechter function. Note that at $z = 2$ the literature fits for Ilbert+ 13 and Tomczak+14 are actually two separate bins ($1.5 < z < 2.0$ and $2.0 < z < 2.5$) which we simply averaged to get the parameters listed here. The same procedure was used at $z = 3$ for the Ilbert+ 13 data (using bins $2.5 < z < 3.0$ and $3.0 < z < 3.5$) and for Tomczak+ 14 we used the last data bin ($2.5 < z < 3.0$). Rows 2 and 5 through 8 are the literature values of the Schechter fit, while Rows 3 and 4 represent the best fit slopes using local group data and keeping the rest of the Schechter fit paramters fixed to their literature values.

Normalized to I13 (UltraVISTA DR 1)

z	$\alpha_{\rm faint}$ (reference)	$\alpha_{\rm faint}$ (cumulative fit)	$\alpha_{\rm faint}$ (differential fit)	$\log(M^*)$ ($M_\odot$)	Φ_1^* (10^{-3}Mpc^{-3})	α_1	$\log(\Phi^*_{\rm faint})$ (10^{-3}Mpc^{-3})
2	[-1.60]	$-1.48^{+0.05}_{-0.03}$	$-1.43^{+0.06}_{-0.03}$	10.74	0.750	-0.23	0.240
3	[-1.60]	$-1.58^{+0.03}_{-0.04}$	$-1.55^{+0.06}_{-0.03}$	10.75	0.145	0.40	0.145

Normalized to T14 (ZFOURGE/CANDELS)

2	$[-1.41^{+0.26}_{-0.22}]$	$-1.42^{+0.06}_{-0.03}$	$-1.37^{+0.06}_{-0.04}$	10.715	0.375	0.535	0.479
3	$[-1.57^{+0.20}_{-0.20}]$	$-1.50^{+0.02}_{-0.05}$	$-1.49^{+0.07}_{-0.03}$	10.74	0.029	1.62	0.204

Table 2.2: Similar to Table 1 except at $z = 4$ and 5. In this case, both literature reference use a single Schechter fit in place of the double Schechter fit used in the Table 1 references. Our best fit slopes were calculated in the same manner, by keeping $M*$ and $\Phi*$ fixed and leaving α as a free parameter.

Normalized to S15 (CANDELS GOODS-N/CANDELS GOODS-S/HUDF)

z	$\alpha_{\rm faint}$ (reference)	$\alpha_{\rm faint}$ (cumulative fit)	$\alpha_{\rm faint}$ (differential fit)	$\log(M^*)$ ($M_\odot$)	$\log(\Phi^*)$ (10^{-3}Mpc^{-3})
4	$-1.53^{+0.07}_{-0.06}$	$-1.52^{+0.03}_{-0.04}$	$-1.48^{+0.06}_{-0.04}$	10.44	0.301
5	$-1.67^{+0.08}_{-0.07}$	$-1.62^{+0.04}_{-0.03}$	$-1.55^{+0.04}_{-0.06}$	10.47	0.134

Normalized to D14 (CANDELS)

4	$-1.89^{+0.15}_{-0.13}$	$-1.56^{+0.03}_{-0.04}$	$-1.52^{+0.06}_{-0.04}$	10.54	0.189
5	$-1.74^{+0.41}_{-0.29}$	$-1.59^{+0.04}_{-0.03}$	$-1.50^{+0.04}_{-0.05}$	10.68	0.124

The red solid line and associated shaded band in Figure 2 shows the preferred fit for $\alpha_{\rm faint}$ (-1.42) that results from fixing the other parameters of the T14 GSMF and then fitting the implied bound descendants to the cumulative $M_\star^{z=2}$ data from Milky Way satellites. The result is almost indistinguishable from the mass function measured by T14 at $z = 2$. This is remarkable given that we are performing a consistency check ~ 10 Gyr after the epoch observed and ~ 3 orders of magnitude lower in stellar mass than the limit of their survey. If instead we do the fit to the differential mass function we find a preferred value $\alpha_{\rm faint} = -1.37$ for the T14 normalization.

The right panel of Figure 2 shifts the focus to $z = 5$, where the dashed lines show the implied Milky Way mass functions in stars formed prior to this redshift assuming the D14 (blue dashed) and S15 (magenta dashed) GSMFs. The D14 fit, with a steep slope $\alpha_{\rm faint} = -1.74$, over-predicts the known count by an order of magnitude. The S15 GSMF at $z = 5$ is much more consistent with what we see locally. The solid magenta line and associated shading (full halo-to-halo scatter) shows the resultant best-fit $\alpha_{\rm faint}$ ($= -1.62$) when normalized to the other Schechter parameters in S15 (see Table 1). The result is similar to the preferred value in S15 (-1.67), though slightly flatter. Given the significant host-to-host scatter, the difference between our best-fit $\alpha_{\rm faint}$ and the S15 value is not significant, as we now discuss.

Table 1 lists our best-fit $\alpha_{\rm faint}$ values when normalized to I13 and T14 at $z = 2$ and $z = 3$ for both cumulative mass function fits (column 2) and differential mass function fits (column 3). Table 2 lists our best-fit $\alpha_{\rm faint}$ values when normalized to D14 and S15 at $z = 4$ and $z = 5$. The differential fits weight the existence of the (likely rare) Magellanic Clouds less than do the cumulative fits and therefore typically prefer slightly flatter slopes (at the $0.03 - 0.05$ level). For all of the fits we perform we use the average of the cumulative stellar mass functions derived from `ELVIS` to compare to the W14 sample in order to compute the best fit faint end slope. We also compute errors on the faint end slope by fitting to the upper and lower 68 % range of the `ELVIS` hosts (e.g., consider the upper and lower ranges of the

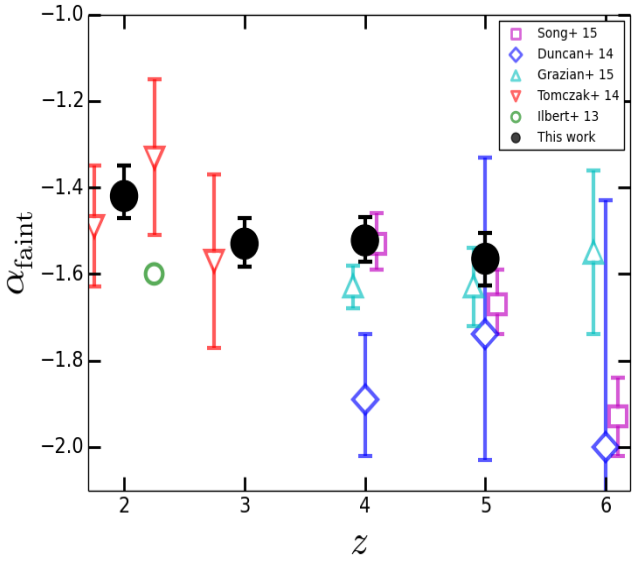

Figure 2.3: Our preferred fits for $\alpha_{\rm faint}$ as a function of redshift (black points) along with recent measurements of $\alpha_{\rm faint}$ from various direct-imaging surveys. The redshifts of the Song et al. (2016) and Grazian et al. (2015) results have been artificially offset for clarity. We include only one point from Ilbert et al. (2013) at $z \simeq 2$ because the faint end slope they adopt is fixed to -1.6 based of their results at $z = 1.5$. Our black points were derived by simply averaging the best fit slopes from Tables 1 and 2 at each redshift. Our error bars include the variance among those four slopes as well as an accounting of halo-to-halo scatter in subhalo abundances.

red band plotted in the upper left panel of Figure 1). This provides an accounting of the expected cosmic variance in subhalo/satellite counts from halo-to-halo.

Figure 3 summarizes our constraints on $\alpha_{\rm faint}$ as a function of redshift and compares our values to recent measurements reported in the literature. We specifically plot the average of the four best-fit $\alpha_{\rm faint}$ values listed in Tables 1 and 2, with errors that treat variance among those four preferred values as systematic combined with the halo-to-halo variance errors listed for each of the four fits. The specific values we prefer are: $\alpha_{\rm faint} = (-1.42^{+0.07}_{-0.05}$, $-1.53^{+0.06}_{-0.05}$, $-1.52^{+0.05}_{-0.05}$, $-1.57^{+0.06}_{-0.06})$ at $z = (2, 3, 4, 5)$.

2.5 Discussion

In this paper we have used near-field observations (deep CMD-based SFHs from W13 and W14) together with ΛCDM simulations to inform our knowledge of the galaxy stellar mass function (GSMF) at early times ($z = 2 - 5$). The power of this approach is that it utilizes a huge lever arm in stellar mass, exploring a mass regime two orders of magnitude below what is currently possible via direct counts. Our results suggest that the low-mass slope of the GSMF must remain relatively flat with only slight steepening over the redshift range $z = 2 - 5$, from $\alpha_{\rm faint}^{z=2} \simeq -1.42^{+0.07}_{-0.05}$ to $\alpha_{\rm faint}^{z=5} \simeq -1.57^{+0.06}_{-0.06}$ at $z = 5$. These constraints are strongly at odds with some published GSMFs, including published estimates that would over-produce local galaxy counts by an order of magnitude or more (see, e.g., the lower right panel of Figure 1).

While the discriminating capacity of this approach is potentially very powerful, there are a few caveats that we must consider. The first is the concern that our simulations may not provide a fair representation of the Milky Way and its local environment. The `ELVIS` hosts we use have virial masses that vary over the range $M_{\rm halo} = 1 - 2.4 \times 10^{12}\ M_{\odot}$. This spans the range of most recent measurements but there are some estimates that fall as low as 7×10^{11} $M_{\odot}$ (see, e.g. Boylan-Kolchin et al., 2013; Wang et al., 2015). If the Milky Way halo mass is really this low, then we would expect roughly a factor of ~ 2 fewer progenitors at fixed halo mass within 300 kpc of the Milky Way. This would shift our median predictions for bound satellite counts down by roughly the same factor for any given GSMF, which is within the shaded regions shown, e.g., in Figure 2. Our preferred faint-end slopes would similarly be systematically steeper, roughly $\alpha_{\rm faint} \rightarrow \alpha_{\rm faint} - 0.05$. Such a shift would not change our conclusion that the preferred low-mass behavior of the I13 and D14 GSMFs are too steep to be compatible with local counts and would not change our conclusions that $\alpha_{\rm faint}$ is evolving weakly to $z = 5$.

A similar concern is associated with the fact that our simulations are pure N-body and lack the additional gravitational potential associated with a central disk. The extra tidal forces associated with the disk will likely liberate mass from some subhalos such that our N-body runs over-predict bound subhalo counts (D'Onghia et al., 2010; Brooks & Zolotov, 2014). We suspect that this effect will marginally affect our work because we count bound structures based on their progenitor masses prior to accretion, not on their masses at $z = 0$ (which will certainly be lower than predicted from N-body for subhalos that orbit close enough to the disk). Progenitor masses will be largely unaffected by the presence of a disk. A more important concern is that more satellites will be completely destroyed when the disk potential is included, thus liberating their stars to the stellar halo (e.g., Bullock & Johnston, 2005a). Given that the total stellar mass of the Milky Way's stellar halo is quite modest ($\sim 10^9\ M_\odot$) compared to the integrated mass of the stellar mass functions shown in, e.g., Figure 2, there is not much room to hide additional mass in tidally destroyed galaxies that are not already accounted for in current N-body based models (Lowing et al., 2015). More work needs to be done in order to solidify this expectation (see, e.g. Brooks et al., 2013, for a promising approach).

Another issue that could affect our results is that we have chosen to use one-to-one abundance matching at $z = 2-5$ in order to assign ancient stellar masses to the progenitors of our bound subhalos at $z = 0$. Some authors have argued that there is actually significant scatter in the abundance matching relation at these low masses (Sawala et al., 2015). Imposing significant scatter in the $M_\star - M_{\rm halo}$ relation could affect our constraints. By definition, any imposed scatter would result in a GSMF that is identical (on average) to those used in the paper; once scatter is imposed, the median $M_\star - M_{\rm halo}$ needs to become steeper in order to result in the same overall number density (e.g., Garrison-Kimmel et al, in preparation). This means that the *median* constraints on $\alpha_{\rm faint}$ would remain the same, but the uncertainty caused by host-to-host scatter would increase accordingly. In order to better understand the effect scatter would have on our results we performed a simple experiment, calculating cumulative stellar

mass functions in the same manner, but allowing the stellar mass given by our abundance matching relations to scatter by 0.2 dex according to a log-normal distribution. The resulting best fit faint end slope shifts as anticipated, however the shift is small (about $\pm$ 0.01). The reason the results are so robust is that each halo has an equal probability of scattering up in stellar mass as scattering down. Every subhalo of the Milky Way would need to have systematically scattered in one direction preferentially to significantly alter our results. Given this, one may ask whether any degree of scatter in the $M_\star - M_{\rm halo}$ relation could enable a D14 stellar mass function to occasionally produce a Milky Way satellite system consistent with the one observed. In order to explore this we have run 10^6 Monte Carlo realizations with 2.0 dex of scatter about a D14-matched relation at $z = 4$ and find that every realization over produces the Milky Way stellar mass function. The lowest overall count of satellites out of 10^6 D14 realizations was 35 objects with $M_{star} > 10^5\ M_\odot$. We conclude that our results are robust to even large amounts of scatter.

While a number potential caveats need to be understood before we can gain further accuracy and precision on our constraints, this paper (along with B14 and B15) has illustrated the potential power of near-field data sets in constraining science that is traditionally relegated to deep field approaches. None of the concerns we have discussed can account for the discrepancy between Milky Way satellite counts and the D14 GSMF at $z = 4$ (see Figure 1); a mass function as steep as $\alpha_{\rm faint} \simeq -1.9$ at $z = 4$ is effectively impossible to reconcile with our current understanding of structure formation.

There are other lines of evidence from the near-field that can inform our understanding of the relationship between halo mass and stellar mass (and thus galaxy abundances) at high redshift. For example, it has been known for some time that reionization will likely shut down galaxy formation below a critical halo mass scale of about $\sim 10^9 M_\odot$ (Efstathiou, 1992b; Shapiro et al., 1994) and that this might leave imprints on the count and star-formation histories of Local Group galaxies that reside within those small halos (Bullock et al., 2000;

Ricotti & Gnedin, 2005; Gnedin & Kravtsov, 2006; Bovill & Ricotti, 2009). The shaded grey band in the lower left panel of Figure 1 corresponds to the halo mass scale where galaxy formation is expected to be suppressed by the external UV ionizing flux at $z = 4$ according to Okamoto et al. (2008). The D14 abundance-matching relation would suggest that we should begin seeing the effects of reionization suppression in galaxies as massive as $M_\star = 10^6$ $M_\odot$ at $z = 4$; however, no systematic truncation in star formation at this epoch is seen in the CMD-derived SFHs of galaxies this massive (W13, W14). The steeper S15 relation, on the other hand, would suggest that UV suppression sets in at the stellar mass regime of ultra-faint dwarfs ($M_\star \sim 10^4$ $M_\odot$). This expectation, which only holds for flatter stellar mass functions as preferred by S15 (and our own work), agrees very well with recent observations that have seen uniformly old stellar populations in ultra-faint galaxies (Brown et al., 2014) and recent simulations (Oñorbe et al., 2015; Wheeler et al., 2015) as well. More data will be needed to confirm whether this dividing line between uniformly ancient stellar populations and continued star formation is sharp at the stellar mass scale of ultra-faint dwarfs, but it is clear that the SFHs of local dwarf galaxies have a lot to tell us about the physics of galaxy formation at early times.

Finally, it is worth stressing the major assumption of this work, and the general concept of using the Local Group as a time machine, which is that the galaxies of the Local Group filled a much larger volume at high redshift, and thus are a representative sample of the dwarf population as a whole at high redshift. It is possible that this assumption is not correct and that dwarf galaxies that are destined to fall into the Local Group are somehow biased with respect to the bulk of the population at high redshift. Future direct surveys of the high-redshift universe that allow deeper constraints on $\alpha_{\rm faint}$ will provide a test of this idea. If future counts measure different values of $\alpha_{\rm faint}$ than we anticipate from near-field studies, then this would help us understand how (and why) Local Group dwarfs would be biased relative to the general population of dwarf galaxies – a result that would be important (if true).

The approach adopted here will be further strengthened by more complete observational surveys of the Local Group. In the near term, complete SFHs from M31 dwarfs will be invaluable. Andromeda is believed to have a similar halo mass to the Milky Way, so including an additional constraint from this system will help us account for halo-to-halo scatter in subhalo populations, which dominates the error we report on $\alpha_{\rm faint}$. More generally, with surveys like LSST poised to come on line, the next decade will almost certainly see the discovery of many more dwarf galaxies throughout the Local Volume, pushing our completeness limits to lower stellar masses and more distant radii (Tollerud et al., 2008). These discoveries, and associated follow-up, will further lengthen the lever arm on stellar mass functions and increase the volumes within which these constraints can be applied, thus decreasing cosmic variance uncertainties. The same instruments that promise to reveal the high redshift universe directly (e.g., *JWST*, TMT, GMT, E-ELT) will also facilitate indirect constraints on these epochs via archeological studies in the very local universe.

Chapter 3

Subhalo destruction and its impact on substructure lensing results

3.1 Introduction

One key prediction of the current paradigm of galaxy formation is that there should be some dark matter halo mass below which galaxies are unable to form (Klypin et al., 1999; Moore et al., 1999; Bullock & Boylan-Kolchin, 2017). For example, if the (cold) dark matter particle is a neutralino, then substructure should exist down to masses of order 10^{-6} $M_{\odot}$, depending on details of the model (Green et al., 2004). The halo mass at which galaxy formation is cut off should be many orders of magnitude higher than this. The specific cutoff scale depends on the complicated interplay between gas cooling and heating by an ultraviolet background but current estimates suggest that the mass scale is between 10^8 and 10^9 $M_{\odot}$ (Efstathiou, 1992a; Bullock et al., 2000; Bovill & Ricotti, 2009; Sawala et al., 2016b; Oñorbe et al., 2016). The implication is that if Cold Dark Matter (CDM) is the correct model, there should be numerous small dark matter halos with no galactic counterparts. As there is currently no

detection of a dark matter particle the presence of such dark halos is a great way to constrain dark matter models.

Low-mass dark halos that exist within the virial radius of larger halos are known as subhalos and many techniques have been proposed to detect them. These include searches for gaps or other features in stellar streams in the Galactic halo (Johnston et al., 2002; Ibata et al., 2002; Carlberg, 2009; Bovy et al., 2016), and via the detection of products in the annihilation of dark matter particles into standard model particles (Kuhlen et al., 2008; Ng et al., 2014; Sánchez-Conde et al., 2011). One additional promising avenue for detecting dark substructure is from strong lensing (Mao & Schneider, 1998; Metcalf & Madau, 2001; Dalal & Kochanek, 2002).

The detection dark substructure via lensing is in principle straightforward. First, a suitably lensed object is detected, the foreground lens is modeled with a smooth potential for the host galaxy, and then perturbations are added to the foreground lens model in the form of potentials of possible dark matter substructure. Several systems have been analyzed with the hopes of detecting a subhalo, resulting in the detection of dark matter substructure at the $\sim 10^9$ $M_\odot$ mass scale for galaxy-galaxy lensing (Vegetti et al., 2012; Hezaveh et al., 2016), and $\sim 10^{7.5}$ $M_\odot$ from quasar flux ratio anomalies (Nierenberg et al., 2014). This has allowed the authors to put constraints on the subhalo mass function and the fraction of mass that is in substructure. With current technology these methods could push down even further to $M_{600} \sim 10^7$ $M_\odot$, however no structures that small have been detected (Nierenberg et al., 2017).

The field of substructure lensing is intriguing because there is great potential in the near future for a substantial increase in the number of lenses and the ability to detect smaller objects. The Dark Energy Survey (DES), LSST, Euclid, and WFIRST will lead to an enormous increase in the number of lensing systems appropriate for looking for dark substructure. As an example, Collett (2015) estimates that DES, LSST and EUCLID will potentially discover

2400, 120,000 and 170,000 galaxy-galaxy lensing systems respectively. Currently, ALMA has the capability to detect very small substructure, potentially probing subhalo masses of 10^6 $M_\odot$ (Hezaveh et al., 2016). Furthermore, JWST will allow for detections at ($\simeq 10^7$ $M_\odot$) in halo mass, based on quasar flux ratio anomalies (MacLeod et al., 2013). However, without accurate predictions for what is expected within CDM, these observational constraints will never reach their scientific fruition.

Up until just a few years ago, simulating large numbers of galaxies with full hydrodynamics at high resolution was not possible. Therefore, theoretical studies of substructure lensing have used dark-matter-only simulations as their benchmark for comparison (e.g., Vegetti et al., 2014). Recent simulations of Milky Way type galaxies have shown that full hydrodynamic simulations produce significantly fewer bound substructures than their dark matter only counterparts (Brooks & Zolotov, 2014; Wetzel et al., 2016; Zhu et al., 2016; Sawala et al., 2016d; Garrison-Kimmel et al., 2017), with a factor of ~ 2 reduction within the virial radius and an order of magnitude fewer subhalos within ~ 20 kpc of the central galaxy. The primary cause appears to be the enhanced central potential created by the host galaxy: subhalos get destroyed as they approach the central galaxy on radial orbits. While this result is potentially of interest for subhalo lensing, most of the highest resolution simulations have been run at the Milky Way mass scale ($\sim 10^{12}$ $M_\odot$), as opposed to the mass scale used for substructure lensing studies which is closer to halo masses of 10^{13} $M_\odot$. Fortunately, such simulations are just becoming feasible both in zoom-in simualtions (Fiacconi et al., 2016) and in full box simulations, such as the EAGLE simulation (Schaye et al., 2015b), and the Illustris simulation (Vogelsberger et al., 2014a). This allows for studies of lensing substructures in simulations with full hydrodynamics. One example of this is Despali & Vegetti (2016) who use the EAGLE simulation (both dark matter only and full hydrodynamics), and Illustris hydrodynamics simulation to investigate predictions for subhalo lensing. They find that hydrodynamic simulations decrease the average expected substructure mass fractions, as would be expected form results on the Milky Way scale.

The present paper expands upon this past work by presenting the distributions of substructure mass fractions seen in projection along random axes through the host halos in the Illustris and Illustris-Dark simulations. We compare to the distribution inferred from the Vegetti et al. (2014) study as well projected substructure mass functions derived from Hezaveh et al. (2016). We explore how the distributions change as we go from dark matter only to full hydrodynamics to illustrate both average differences between the two and and impact of halo-to-halo scatter on expected substructure detection probabilities.

The format of the paper is as follows. Section 2 details the Illustris simulations, our host sample, and subhalo properties. Section 3 shows our results on substructure mass fractions and subhalo mass functions. Section 4 explores the implications for substructure lensing.

3.2 Simulations and Methods

We make use of the publicly available Illustris simulations (Nelson et al., 2015; Vogelsberger et al., 2014a) for this work and adopt their cosmological parameters: $\Omega_m = 0.2726$, $\Omega_\Lambda = 0.7274$, $\Omega_b = 0.0456$, $\sigma_8 = 0.809$, $n_s = 0.963$, and $h = 0.704$. The Illustris suite consists of three hydrodynamic and three dark matter only (DMO) simulations of increasing resolution all initialized at $z = 127$ in a box that is 106.5 Mpc (co-moving) on a side. We use only the highest resolution version, Illustris-1, which has a dark matter particle mass of $m_{dm} = 6.3 \times 10^6\ M_\odot$ and a gas particle mass of $m_{gas} = 1.3 \times 10^6\ M_\odot$. The DMO version of Illustris-1 subsumes the baryonic matter into the dark matter particles and thus has a DM particle mass $m_{dm} = 7.6 \times 10^6\ M_\odot$. In what follows, when we compare dark matter halo masses from Illustris-1 to those in Illustris-1 Dark we account for the excess baryonic mass in the DMO run by multiplying halo masses by $(1 - f_b)$, where $f_b \equiv \Omega_b/\Omega_m = 0.167$. This approach assumes that the dark matter (sub)halos of interest are effectively depleted of their baryons. For the sake of brevity, we refer to the Illustris-1 and Illustris-1 Dark simulations as simply

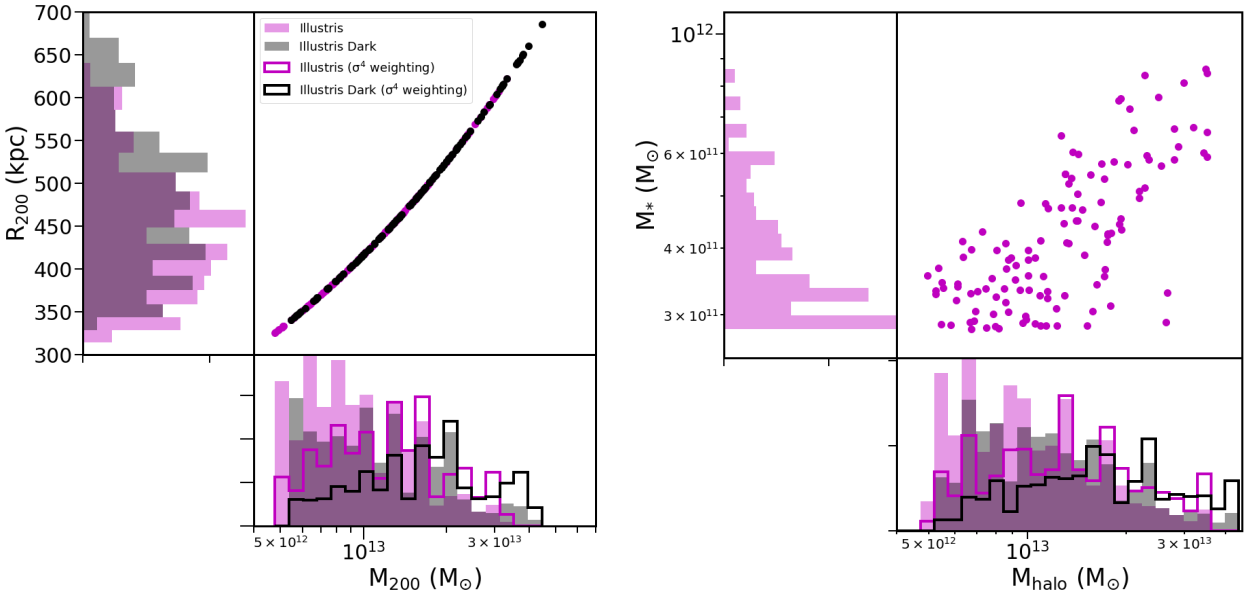

Figure 3.1: Properties of the host halos of our mock lens sample taken from Illustris and Illustris Dark selected such that they are isolated (as described in text) and that they are identified as the same halo in both Illustris and Illustris Dark. Left: M_{200} versus R_{200} for the sample. Right: M_{halo} versus galaxy stellar mass $M_\star$ (for Illustris). The shaded histograms represent the fiducial sample, and the unfilled histograms represent the results of weighting the systems by σ^4, reflecting the fact that systems for which a multiply lensed galaxy is detected are biased towards larger halos (see Section 2). Note that while M_{200} and M_{halo} are similar, they are noticeably different (see section 2.1 for definitions of these two masses).

"Illustris" and "Illustris Dark" below.

3.2.1 Host halo selection

Dark matter halos in the Illustris catalogs were derived using a friends-of-friends (FoF) algorithm with a linking length of 0.2 times the mean inter-particle separation. After these FoF halos were identified, SUBFIND (Springel et al., 2001) was run on them in order to identify substructures around the host halos. For the rest of this work, we rely on two of the halo mass measurements provided in the Illustris data release. The first of these masses is M_{200}, which is defined as the total mass enclosed in a sphere of radius R_{200} that has a mean density 200 times the critical density of the universe. The second mass parameter,

which we refer to as $M_{\rm halo}$, is the mass that is bound to that halo but not bound to any of its subhalos. In general, we will use M_{200} when discussing the host halos, and $M_{\rm halo}$ when discussing subhalos. We will also refer to halos and subhalos in terms of their $V_{\rm max}$, which is the maximum circular velocity of the halo. In our substructure analysis, we consider every subhalo within R_{200} of the host and usually consider only subhalos with $M_{\rm halo} > 10^9\ M_\odot$ (with more than 130 particles) in order to ensure completeness.

Our aim is to explore substructure in massive halos of the type associated with strong-lens systems focusing on the distribution of mass fractions, and substructure mass functions. As a benchmark, we refer to the sample used in Vegetti et al. (2014), which has an average redshift of of $\langle z \rangle = 0.233$ and consists of galaxies with stellar masses $M_\star = 10^{11.45-11.95}\ M_\odot$. Motivated by this, we focus our study on galaxy halos in the the $z = 0.2$ Illustris snapshot that host galaxies in this stellar mass range. We also make sure that the subhalo containing the galaxy is the most massive system in its FoF group, this works as a rough isolation criteria. We then create a matched DMO sample by using matching files provided in the public Illustris data release to match to Illustris Dark. This leaves us with a lens host sample of 122 halos in both Illustris and Illustris Dark. Figure 3.1 shows the basic properties of our host galaxy-halo sample, with the dark matter only halo masses corrected by the baryon fraction (1-f_b). Interestingly, even after the hosts from Illustris Dark are corrected for the baryon fraction, they still end up being slightly more massive than the matched sample from Illustris. This may be associated with the dynamical loss of dark matter in response to explosive feedback episodes (Taylor et al., 2016).

Our sample of simulated galaxies covers the same stellar mass as the Vegetti et al. (2014) lens sample, with a M_{200} range of 5×10^{12} to $4 \times 10^{13}\ M_\odot$. In terms of $V_{\rm max}$, this translates to halos between 300 and 700 km s^{-1}. Note that while our sample has been selected from the same stellar mass range as the Vegetti et al. (2014) sample, it has a different distribution. This is because while there are more galaxies at smaller masses, galaxies at larger masses

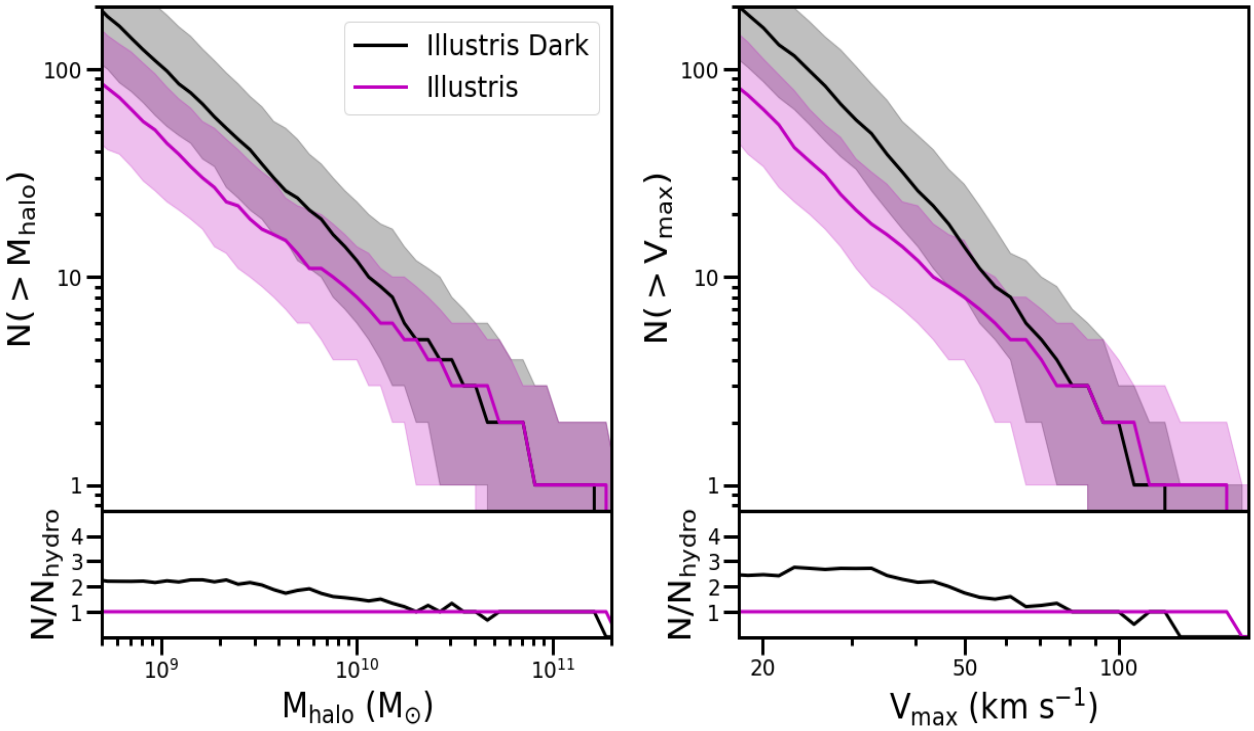

Figure 3.2: Median subhalo mass functions (left) and $V_{\rm max}$ functions (right) for our host galaxy samples from Illustris (magenta) and Illustris Dark (black). Lines show medians, with 68% shown as shaded bands. As emphasized in the lower panels, the DMO runs contain roughly twice as many subhalos as the hydrodynamic runs.

are more likely to be strong lenses. In order to account for this, we weight the distribution of galaxies by σ^4, where σ is the velocity dispersion of halo. This is roughly how lensing strength scales with increasing mass (Bourassa et al., 1973), and once correcting for this effect, our distribution of stellar masses looks similar to that from the Vegetti et al. (2014) sample. The resulting distribution is shown in Figure 3.1. For the rest of this work, we will weigh our samples by the same factor.

3.2.2 Subhalo selection

For the substructure, we restrict ourselves to the Illustris subhalo catalogs and subhalos with a mass $\geq 10^9 M_\odot$. Furthermore, we restrict ourselves to halos within R_{200} of the host halo.

However, It is important to note that small halos along the line of sight to a lens could also cause perturbations and also influence the lensing signal (Metcalf, 2005; Despali et al., 2017).

One important issue concerns the definition of subhalo mass. There are at least two separate classes of mass ambiguity important for substructure lensing studies. The first has to do with translating a reported subhalo mass from a lensing analysis to a subhalo mass as measured in a simulation. The second has to do with how one defines subhalo mass in a simulation from the outset. We refer the reader to Minor et al. (2016) for a discussion of how the shape of the assumed perturber's density profile affects strongly the mapping between the mass reported for a subhalo in simulations and the mass usually assumed in lensing models. The second issue is explored in Appendix 3.4, where we show that different halo finders can lead to a factor of ~ 2 differences in subhalo mass functions derived for the same simulation. As we move towards an era where strong lenses suitable for substructure constraints become more common, the community will need to agree upon the best way to characterize subhalos and their masses to make progress in constraining the nature of dark matter or galaxy formation on small scales. In this paper we adopt the subhalo masses as defined in the primary Illustris catalog.

We note that the Illustris catalogs contain a few low-mass items in the subhalos catalogs (about one per host) that are fully baryon-dominated (with more than 50% of the total mass baryonic). These unusual systems are typically found close to the central galaxy (see Appendix 3.5) and are potentially associated with SUBFIND identifying part of the host galaxy as a separate galaxy subhalo. In general, these baryon-dominated halos tend to be star particle dominated at very small radii ($r < 10$ kpc) and gas dominated further out (10 kpc $< r < 25$ kpc). For the rest of this analysis, we throw out any baryon-dominated subhalos because we are interested only in prospects for detecting actual dark matter substructure. However, it is worth noting that any real clumps of gas or stars (e.g. star clusters, tidal dwarf galaxies, or gas clouds) in the vicinity of lens hosts could be a significant background in lensing searches

for dark substructure. Studies of this effect have estimated the contamination to be about 10% although the specifics depend on the lens method, and the mass of the perturber (Hsueh et al., 2017a; Gilman et al., 2017; He et al., 2017).

3.3 Results

The left panel of Figure 3.2 shows subhalo mass functions (within R_{200}) for our Illustris (magenta) and Illustris Dark (black) host samples. The lines show median values and shaded bands show 68 percentile confidence intervals. Subhalo masses in Illustris Dark have been scaled $M_{\rm halo} \rightarrow (1-f_b)M_{\rm halo}$ in order to account for the baryonic mass subsumed by the 'dark matter' particles in the DMO run. The right panel of Figure 3.2 shows the corresponding subhalo $V_{\rm max}$ functions (again with $V_{\rm max} \rightarrow \sqrt{1-f_b}V_{\rm max}$ in the DMO runs). The full physics runs display fewer subhlaos in both presentations. The bottom panels quantify the difference by showing the ratio of subhalo counts in the DMO simulations to the hydrodynamic simulations. The hydrodynamic simulations have about a factor of two fewer subhalos at fixed subhalo mass than the DMO simulations, even after accounting for baryonic mass loss.

In addition to having fewer subhalos at a given mass, the full hydrodynamic simulations appear to have a different shape in the subhalo mass function. Previous work has reported that hydrodynamic simulations and DMO simulations have different slopes (Despali & Vegetti, 2016; Chua et al., 2016), but our results suggest a more nuanced difference. Interestingly, the mass functions for the full hydrodynamic run seems to match the DMO simulations at high masses ($M_{halo} > 2 \times 10^{10}\ M_{\odot}$) and to have the same slope at low masses. The only real difference in slope is in the intermediate mass regime ($M_{halo} \simeq 10^{10}\ M_{\odot}$; $V_{max} \simeq 40$ km/s), indicating a mass range where subhalo destruction may be most efficient, and potentially indicating that fitting halo mass functions with a single slope may not be entirely accurate.

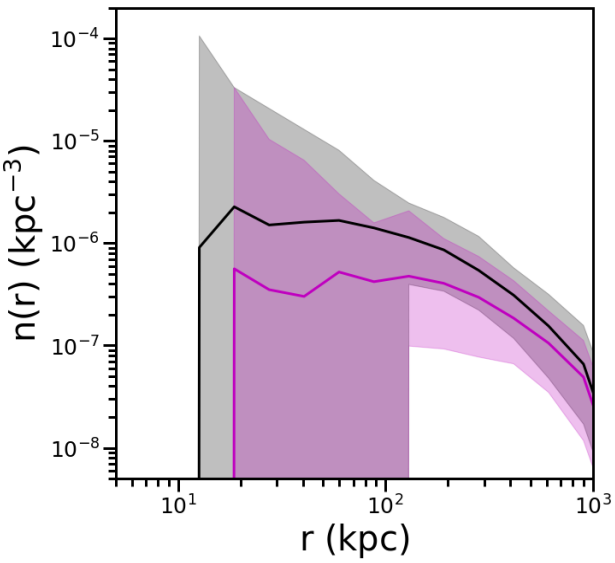

Figure 3.3: Average 3D radial distributions of dark subhalos more massive than $M_{\rm halo} = 1 \times 10^9\ M_\odot$ in Illustris (magenta) and Illustris Dark (black) as a function of radius r. Shown are averages over all host halos in our large sample of hosts. Not only is the overall count of subhalos reduced in the hydro runs, but their radial distribution is less centrally concentrated. This strongly suggests that dynamical disruption of substructure from the central host galaxy plays a major role reducing substructure counts compared to the DMO simulation.

What is the cause of this substructure depletion? As seen in previous work focusing on Milky Way size halos (Brooks & Zolotov, 2014; Wetzel et al., 2016; Zhu et al., 2016; Sawala et al., 2016d; Garrison-Kimmel et al., 2017), the origin appears to be subhalo interactions with the central galaxy. Evidence for this is presented in Figure 3.3, which shows the average differential number density of subhalos as a function of radius in the DMO (black) and full physics (magenta) samples. Here we include all subhalos more massive than $M_{\rm halo} = 10^9 M_\odot$. We see that not only are there fewer subhalos in Illustris compared to Illustris Dark, but the radial distribution is significantly depleted in the central region. There is a sharp cutoff in dark subhalo counts within $r \simeq 20$ kpc, which we attribute to interactions with the central host galaxy. This lack of expected dark subhalos at small radius could potentially be important for substructure lensing studies, which are sensitive to subhalos at small projected radius, comparable to the host lens Einstein radius (typically $\lesssim 10$ kpc). We explore implications for lensing explicitly in the next subsection.

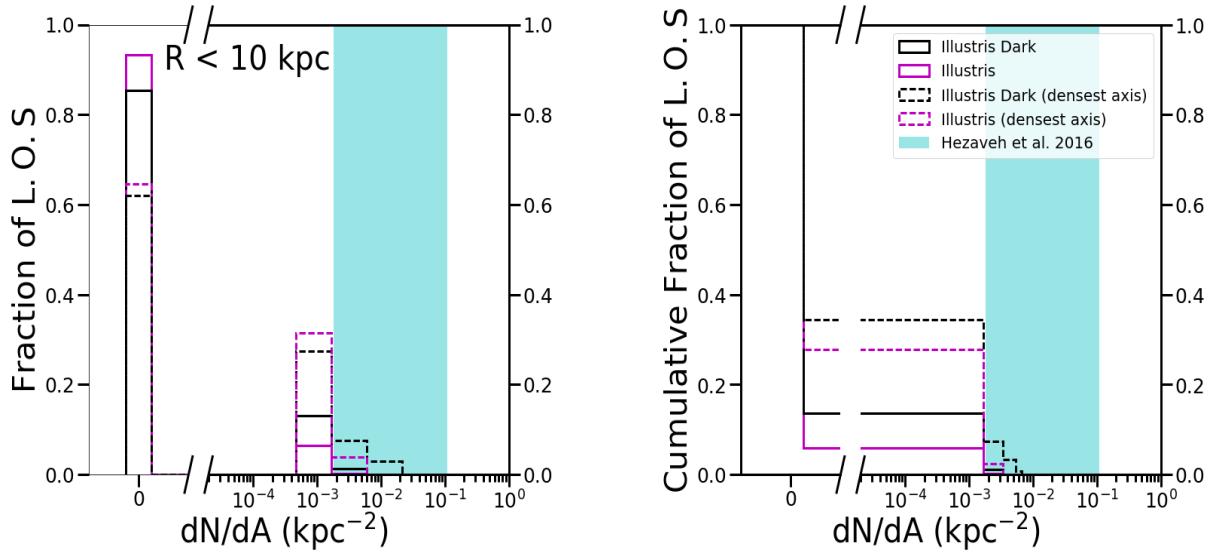

Figure 3.4: Subhalo surface number density distributions. Left: Fraction of projections through our Illustris (magenta) and Illustris Dark (black) halos that contain a given number of subhalos per unit area. The bin on the far left corresponds to projections with no substructure. We count only subhalos with $M_{\rm halo} > 10^9$ M$_\odot$ in cylinders of radius $R = 10$ kpc, which is typical (though somewhat larger) than an Einstein radius for strong lenses of this type. The solid lines show results when each halo is viewed along 100 random projections through the halo. The dashed lines include one projection per halo, viewed along each host halo's densest axis. Right: the same distributions shown cumulatively. The shaded regions in both panels show the substructure surface density derived from Hezaveh et al. (2016) for the same subhalo mass cut. The simulated halos typically have lower substructure fractions than observed, with many projections containing no subhalos at all. This is especially true for the full physics simulations.

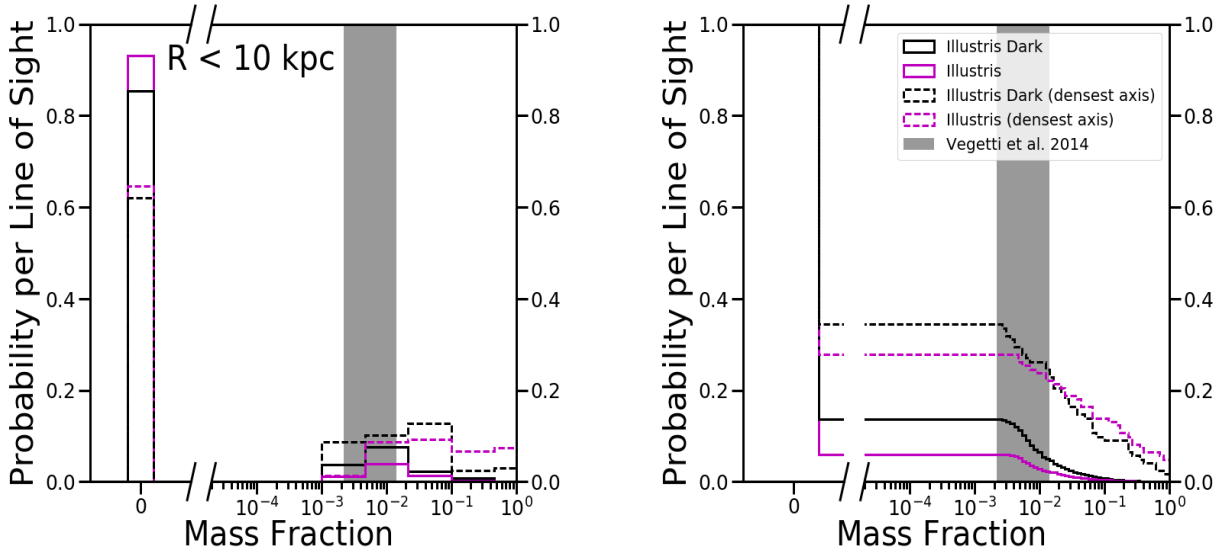

Figure 3.5: Subhalo mass fraction distributions. Left: Fraction of projections through our Illustris (magenta) and Illustris Dark (black) halos that contain a given mass fraction in substructure within cylinders of radius $R = 10$ kpc with length $L = 2 \times R_{200}$. Right: the same distributions shown cumulatively. We have counted the mass in subhalos $M_{\rm halo} > 10^9$ $M_\odot$ whose centers sit within the cylinder. The grey shaded region corresponds to the reported results of Vegetti et al. (2014). The solid lines show results when each halo is viewed along 100 random projections through the halo. The dashed lines include one sightline per halo, viewed along each host halo's densest axis.

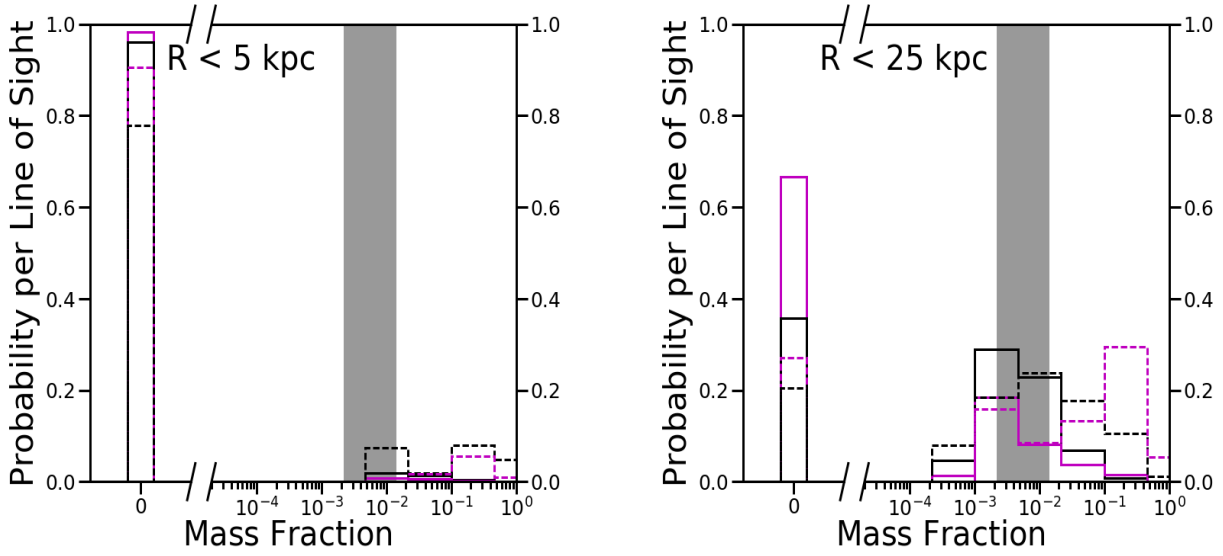

Figure 3.6: The same as figure 5 except varying the assumed projected radius. Predictably, changing the radius to 5 kpc drastically lowers the projections with a detected substructure, while increasing to 25 kpc increases it.

3.3.1 Implications for subhalo lensing

Gravitational lensing studies are sensitive to the projected mass along the line of sight near the lens plane of the host. Substructure constraints are often quoted in terms of the projected mass fraction in substructure (e.g. Dalal & Kochanek, 2002; Vegetti et al., 2014) or the projected subhalo mass function (Hezaveh et al., 2016). We explore predictions for both approaches here.

Figure 3.4 provides a comparison to the results of Hezaveh et al. (2016), who report projected subhalo counts per unit area based on their lensing analysis. For each host halo in our Illustris and Illustris Dark sample, we construct 100 random projections through the halo and count the number of subhalos N more massive than $M_{\rm halo} = 10^9 M_\odot$ within a projected cylinder of radius $R = 10$ kpc and length $L = 2 \times R_{200}$ through the halo. For the full hydrodynamics run we include subhalos whether or not they have an obvious stellar component. The fraction of projections that have a given subhalo count per unit area is shown as a histogram on the left and cumulatively on the right, with solid black lines corresponding to the DMO simulation and solid magenta lines corresponding to the hydrodynamical simulation. We see that the vast majority of projections in the Illustris sample ($\sim 95\%$) include no subhalos above our mass cut within this projected radius. The fraction of empty projections drops only slightly to $\sim 85\%$ in the Illustris Dark sample.

The cyan bands show the reported projected subhalo count from Hezaveh et al. (2016), where the width of the band represents the 95% confidence interval [1]. The Hezaveh et al. (2016) range is noticeably offset from the distribution seen in Illustris, with more substructure than would be expected along a typical projection. Only $\sim 0.25\%$ ($\sim 1\%$) of the projections from Illustris (Illustris Dark) are consistent with the reported counts. One possible reason for this is that a halo is more likely to be a strong lens if it is viewed along its major axis towards the

[1] Hezaveh et al. report a differential mass function per unit subhalo mass. We have derived the gray band by integrating their mass function to 10^9 $M_\odot$, assuming their reported power law.

observer. The dashed lines in Figure 3.4 shows results if we restrict each halo to be viewed only along its densest axis. With this restriction, the fraction of projections consistent with the Hezaveh et al. (2016) range increases to $\sim 2.5\%$ (7%) and the fraction of empty cylinders drops to $\sim 65\%$ in Illustris and $\sim 72\%$ in Illustris Dark. It is important to note that while the vast majority of our projections through the halo produce no detections, the comparison to the Hezaveh range is not an ideal one given the observational range was based on a single detection, additionally the Hezaveh et al. (2016) system is at a higher redshift $z = 0.299$, and thus the system could not have had enough time to destroy a significant amount of substructure. We now turn to the larger comparison set of Vegetti et al. (2014).

Figure 3.5 shows a similar analysis to that presented in Figure 3.4, now recast for comparison to the substructure mass fraction results reported in the gravitational imaging analysis of 11 systems reported in Vegetti et al. (2014). We use the same procedure as outlined in the comparison to Hezaveh et al. (2016), however now instead of only counting the number of subhalos detected above 10^9 $M_\odot$ we explicitly account for their masses, using only the dark matter mass in the full hydrodynamics run. In order to compute the mass fractions in the simulated halos, we include the mass of all subhalos with centers that lie within the cylinder and divide by the mass of all dark matter particles within the cylinder. This means that there are cases where some fraction of the subhalo mass that sits outside the cylinder's radius is included, but the approach is reasonable because the centers of halos are most important in producing lensing anomalies. The line colors and types mirror those in Figure 3.4 and the grey shaded region shows the distribution from the Vegetti et al. (2014) sample who measured a mass fraction of $f = 0.0076^{+0.0208}_{-0.0052}$. This mass fraction estimate was derived given that they include 11 systems with one detection and a mass fraction for that detection of f = 0.0215 (Vegetti et al., 2010). With this fiducial comparison, we see that the distribution from the Vegetti et al. (2014) is consistent with projections from both Illustris and Illustris Dark within the measured uncertainty. Most of the lensing systems in the Vegetti sample ($\sim 90\%$) include no detected substructure, as expected from the simulations.

Of the projections with a detection, a majority are a single subhalo, meaning the scatter in mass fraction is driven mostly by scatter in the subhalo mass itself. Interestingly, the fraction of empty projections is predicted to be lower than observed if we restrict ourselves to the densest axis projections.

It is important to note that the non-detections depend on the lowest subhalo mass that can be measured, so as techniques and observations improve, the space below mass fractions of $\simeq 10^{-3}$ will be filled in with detections of smaller halos both in the current sample of lenses that can be measured and in lower mass hosts or less dense projections through the halo with lensing efficiencies that are too weak provide a currently detectable signal. Furthermore, there is some ambiguity in this direct comparison due to the different ways that mass fractions are computed from the data, and in this work. In particular the Vegetti et al. (2014) sample mass fractions are computed taking into account many additional factors in a statistical framework including the slope of the subhalo mass function, and a minimum subhalo mass of 4×10^6 $M_\odot$ which is significantly lower than the resolution limit of the Illustris simulations.

There also appears to be mismatch in that the simulations show a tail of very high mass fraction projections. This appears to be partially an artifact of our adding the entire subhalo mass in every subhalo mass fraction estimate in cases where large subhalos sit at the edge of the cylinder. To test this we compute the mass fraction two alternative ways. First, we estimate the total subhalo mass by counting every particle associated with a subhalo that was within the cylinder. This cuts down on adding a significant amount of mass that is outside the cylinder, but with the added problem that often we are counting very low density parts of halos that are outside of the cylinder, which will probably not contribute to the lensing signal. This method reduces the number of non-detections; however, most of these non-detections end up in a tail down to low mass fractions caused by only the outskirts of a halo being within the cylinder, and are most likely not dense enough to cause

a detectable lensing perturbation. The second method is similar, but excludes particles from subhalos that do not have centers within the cylinder. With this method, the mass fraction of systems does decrease by about a factor of 2.

The surface density of subhalos (and subhalo mass fractions) that we expect to see along a given projection through a halo is highly sensitive to the projected radius used. This expectation can be seen in Figure 3.3, where we have shown that subhalos tend to be evacuated near a halo's center owing to tidal destruction. Though surface counts can include halos with large 3D radius that just happen to project within small radii, the effect is still important. Figure 3.6 reproduces the analysis shown in in Figure 3.5 but with cylinders of both smaller ($R = 5$ kpc) and larger (25 kpc) radii. We see that the fraction of projections with zero subhalos increases dramatically for the 5 kpc case and decreases for the 25 kpc cylinder. Typical Einstein ring radii for massive galaxy lenses are ~ 5 kpc (Bolton et al., 2008), so in using $R = 10$ kpc in the discussion above we are biasing our results towards somewhat higher substructure counts than might be expected in observations. The $R = 25$ kpc projections clearly result in much higher mass fractions and fewer empty projections than observed, but this is to be expected given the mismatch between R and typical Einstein ring sizes. Interestingly, the $R = 5$ kpc distribution from Illustris 1 along the densest axis is in better agreement with the Vegetti et al. sample than was the $R = 10$ kpc case, as might be expected. However, the limited force and mass resolution of the Illustris simulations subject the 5 kpc projections to potentially under-predicting substructure at small radius due to over merging. This is why we have used the 10 kpc projections as our fiducial comparisons above.

In summary, given the limited size of the data comparison sample, the predicted substructure fractions seen in both Illustris and Illustris dark appear to be consistent with what has been observed by Vegetti et al. (2014). As sample sizes increase, we would expect observations to more closely align with the predictions of full hydrodynamic simulations if LCDM is indeed the correct underlying model.

3.3.2 Compairison to previous theoretical results

The results of this work appear to be in broad agreement with numerous theoretical results on general subhalo statistics, and more specific analyses relevant for lensing systems. For example, several works have noted the decrease in the subhalo mass function as a result of baryonic processes (Despali & Vegetti, 2016; Garrison-Kimmel et al., 2017; Sawala et al., 2016d; Zhu et al., 2016) and in the halo mass function as a whole Chua et al. (2016); Schaller et al. (2015). This decrease seems to be at the factor of two level, and is present in both $z = 0$ and $z = 0.2$ mass functions implying that subhalo destruction becomes important at $z > 0.2$. In addition, our results are broadly consistent with theoretical results more specifically looking at the comparision between simulations and detections from substructure lensing.

For example, Despali & Vegetti (2016) who used the Illustris and Eagle simulations to compute substructure mass fractions. They measure average mass fractions of $f_{sub} = 0.0044 \pm 0.0018$ for the DMO simulations, $f_{sub} = 0.0025 \pm 0.0012$ for the EAGLE simulation, and $f_{sub} = 0.0012 \pm 0.0004$ for the Illustris simulation. These results are lower than what is measured on average in our analysis, this is potentially due to their framework for estimating the mass fractions which more closely follows the statistical framework used in observational measurements of substructure lensing. This allows them to estimate the contribution of smaller subhalos to the mass fraction than in our analysis, which is limited by the resolution of the simulation. However, due to the large variance between different projections through the halo our results are still broadly consistent. An additional interesting comparison is to results from Jiang & van den Bosch (2017), who used DMO simulations along with a semi-analytic model to measure subhalo mass fractions in halos over a wide range of host halo and subhalo masses. They also find lower mass fractions on average than what is found in our analysis, pointing toward $f_{sub} \leq 10^{-3}$. However, the authors note that the halo-to-halo variance is extremely large the results from Vegetti et al. (2014) are within the 90% confidence interval of their simulations.

3.4 Ambiguity in subhalo masses

Halo finders assign masses to subhalos in different ways, and therefore produce different subhalo mass functions even when applied to the same simulations. We illustrate this problem by analyzing our Illustris Dark halo sample using three different halo finders. In addition to the default Illustris halo finder SUBFIND (Springel et al., 2001), we use Rockstar (Behroozi et al., 2013a) and Amiga Halo Finder (AHF; Knollmann & Knebe, 2009). Each of these these halo finders work in different ways, and we refer the reader to the specific papers for in depth explanations of their differences. We provide a short description of each method below.

Rockstar works by running a 3D FoF algorithm to identify overdensities, and then a 6D phase space algorithm is run to identify halos, the linking length is adaptively tuned so that some fraction (by default 70%) of the particles in that group are linked together with at leasts one other particle. Seed halos are placed at the bottom of those groups with particles assigned to their closest seed. Finally, unbinding is performed, and then subhalo properties are calculated. In AHF, dark matter structure and substructure is identified via a grid, where the grid is refined iteratively based on the local density. In practice, if there are more particles in a cell than a number which can be set by hand, the cell is divided in half and the process is repeated. Once this procedure is finished, the most dense areas are called the halo centers and particles are assigned to those halo centers. Finally, unbound particles are removed iteratively, with particles moving at some multiple of the escape velocity (by default $1.5v_{esc}$) removed. In contrast to these, the default Illustris halo finder is SUBFIND. SUBFIND is based on a hierarchical Friends of Friends (FoF) algorithm, where the FoF linking length is reduced in discrete steps. Within the FoF group, a smoothing kernel is used to estimate the density within the group. Any locally overdense area of the FoF group is labeled a substructure candidate, and once the algorithm has identified all locally overdense regions, it assigns dark matter particles to those candidates, and undergoes an unbinding

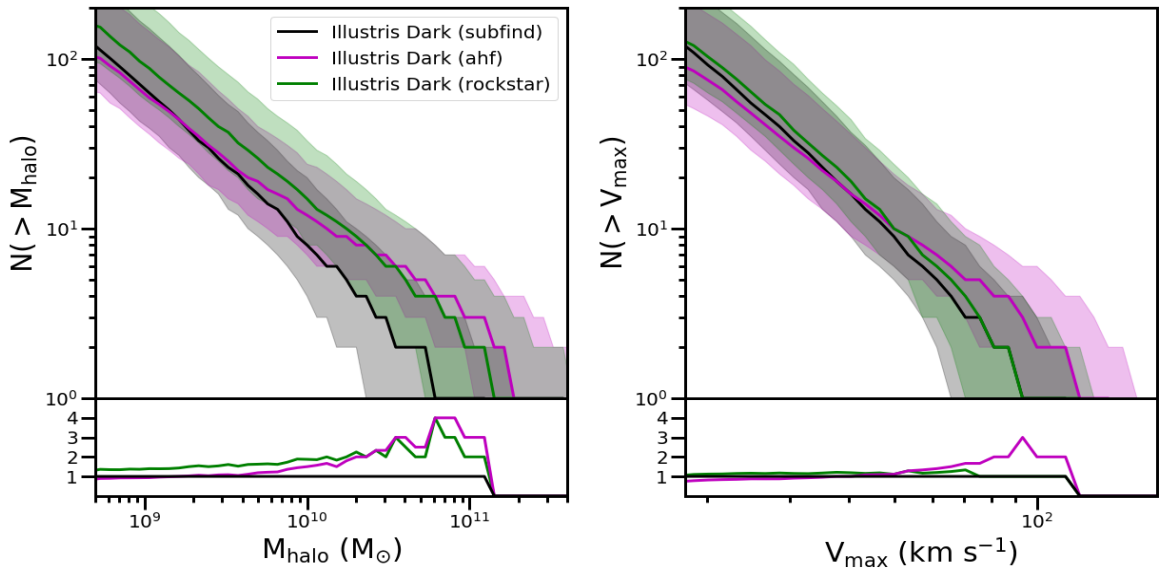

Figure 3.7: The subhalo mass functions (left) and subhalo V_{max} functions (right) for the galaxies in our sample compared between different halo finders (AHF and ROCKSTAR) run with their fiducial parameters.

procedure eliminating unbound particles. If the remaining candidate has enough particles in it to pass some pre set threshold (32 in Illustris), it is counted as a subhalo.

The subhalo mass functions are shown in the left hand panel of Figure 3.7 for Illustris Dark. In general, the fiducial Illustris halo finder (SUBFIND) has the lowest abundance of halos, and Rockstar the highest, with AHF somewhat in the middle, although the halo mass function produced by AHF seems to have a different slope. This disagreement can be due to two competing reasons; either the halo finders are finding different populations of halos, or they are finding the same populations of halos but assigning them different masses. We argue that the significant disagreement can be almost completely attributed to assignment of particles to halos. This can be illustrated by looking the associated V_{max} function (right panel of Figure 3.7). While the agreement is not perfect, it is significantly better than in the halo mass functions and this implies that it is mainly a mass definition issue, and not that the halo finders are identifying different populations of halos. We have additionally run the halo finders on the full hydrodynamics simulations and find similar differences between

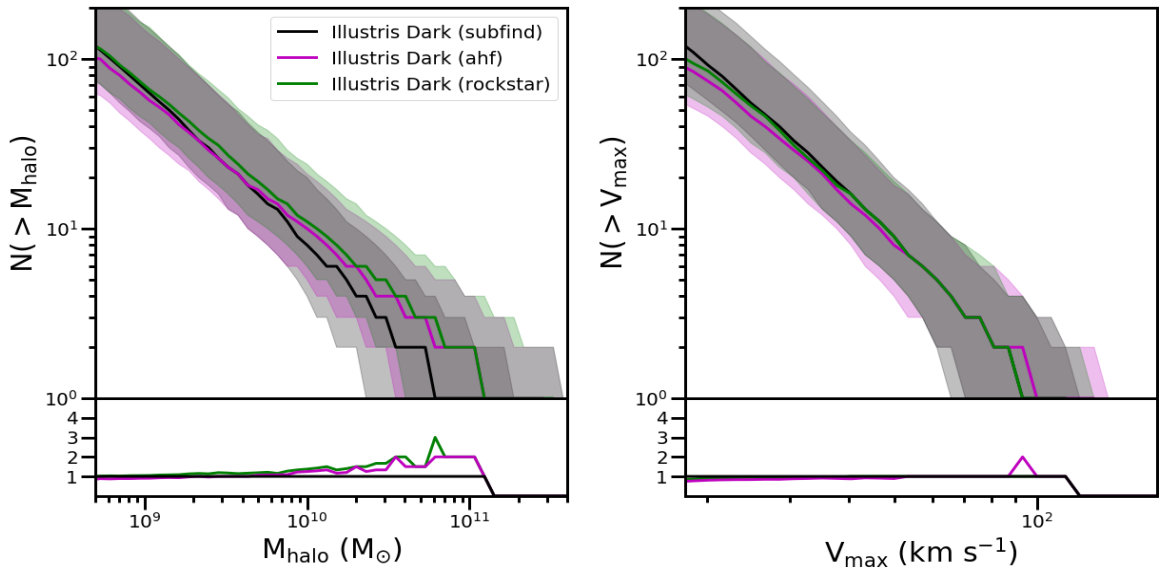

Figure 3.8: Same as in figure A1; however, the fiducial parameters for ROCKSTAR and AHF have been modified. First, the velocity at which particles are determined to be unbound in AHF was lowered to 1.25 v_{esc} (from the default 1.5 v_{esc}) and the binding criteria for rejection in Rockstar was modified to 95% (from the default 50%).

halo finders. This is particularly interesting as this implies the offset between Illustris and Illustris Dark seen in Figure 3.2 is preserved regardless of what halo finder is used.

The differences in the mass assignments can be attributed to different ways in which the halo finders assign bound particles. AHF and SUBFIND use a 3D algorithm with an iterative unbinding criteria. Rockstar calculates the fraction of particles that are bound to the halo, and if it is within some acceptable tolerance (by default 50% bound fraction), the halo is accepted; if not it is thrown out. To test this idea, we can modify the binding criteria of AHF and Rockstar. This is illustrated in Figure 3.8. Here we set the AHF binding criteria to reject particles moving faster than $1.25v_{esc}$ (where the the default $1.5v_{esc}$). We have modified Rockstar to reject halos that have more than 95% of their particles unbound (raised from the default 50%). Once this is done, we see much better agreement between the three halo finders.

The above exercise illustrates that subhalo mass is a fairly subjective measure and there-

fore not an ideal choice for direct comparisons subhalo lensing studies. When subhalos are counted using their V_{max} values, the results are in much better agreement between halo finders. This is because V_{max} probes the inner regions of the halo, and is therefore less sensitive to bound versus unbound particles. As the field moves towards more precise comparisons, V_{max}, or similarly the mass within some small radius, will be a robust parameter with which to compare simulations and observations. This is similar to what is advocated by Minor et al. (2016).

For a more thorough analysis of the difficulties involved in halo finding, particularly in defining halo masses, we refer the reader to Knebe et al. (2011), who carried out a much broader comparison of halo finders and echo the sentiment that a parameter such a V_{max} should be used in place of halo mass. Additionally, we refer the reader to the subhalo comparison project (Onions et al., 2012) who looked at a variety of halo finders and their ability to recover subhalos around Milky Way-like galaxies. Similar to our analysis they find that the halo finders agree in general in identification of subhalo positions, but masses (and therefore mass functions) can vary on the level of 20%.

3.5 Baryon Dominated Substructures

It is possible that baryonic clumps rather than dark matter clumps will be detected in strong lensing searches for substructure. Concern for such a scenario was raised by Gilman et al. (2017) and Hsueh et al. (2017a), who showed that luminous substructures can cause anomalous lensing signals in theory, and potentially confirmed by Hsueh et al. (2017b), who found a flux ratio anomaly from an edge-on disk.

As mentioned in Section 2, there are several baryon-dominated structures listed as subhalos in the Illustris catalogs among our sample of 122 galaxy hosts. Figure 3.9 shows the radial

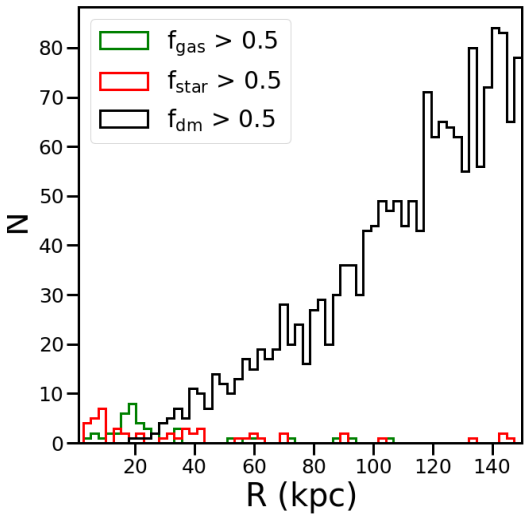

Figure 3.9: Objects from the SUBFIND subhalo catalog within 150 kpc of all of the systems selected from Illustris above 10^9 $M_\odot$ in halo mass. The histograms are colored by the most dominant particle in the object, red if the stellar mass is over 50% the total mass, green if the gas mass is over 50% of the total mass, and black if the halo is dark matter dominated.

distribution of all of the subhalos in our fiducial sample stacked together. The green and red histograms show gas-dominated and star-dominated systems, respectively, while the black histogram shows dark-matter dominated subhalos. There are about 100 baryon-dominated "subhalos" out of $\sim 10,000$ subhalos in total. Most of them exist within the central ~ 20 kpc of the galaxy. We have chosen to remove these systems from our analysis, which focuses on predictions for *dark* substructure. If the majority of these baryonic substructures are "real" predictions – as apposed to spurious numerical artifacts associated with halo finding in the vicinity the galaxies themselves – they would need to be treated as foregrounds in any dark subhalo search.

3.6 Conclusion

In this paper, we have used the Illustris simulations (Nelson et al., 2015; Vogelsberger et al., 2014a) to investigate the dark substructure content of dark matter halos chosen to be rep-

resentative of those studied in substructure lensing analyses ($M_{\rm halo} = 0.5 - 4 \times 10^{13}$ $M_\odot$; see Figure 3.1) and explored how substructure content changes from the dark-matter-only run of Illustris Dark to the full physics run of Illustris. Our sample consists of more than 100 such host halos at $z = 0.2$ and we use them to make projections for substructure lensing studies, specifically for the detection of substructures more massive than 10^9 $M_\odot$, comparable to reported detections (Vegetti et al., 2014; Hezaveh et al., 2016).

We find that the addition of full hydrodynamics reduces the over all subhalo mass function within the virial radius of typical lens-host halos by about a factor of two (Figure 3.2), an effect that appears to be driven by enhanced central destruction caused by the additional central host galaxy potential (Figure 3.3). Naively one would expect this to translate to a factor of two decrease in the expected substructure mass fraction to be observed in lensing studies. However, when viewed in projection to mimic the lensing signal, the large halo-to-halo scatter leads to a more nuanced prediction (Figures 3.4-3.6). Specifically, most projections through the halo of size close to an Einstein radius contain no substructure at all. For cylinders of radius $R = 10$ kpc, the fraction of empty projections rises from $\sim 85\%$ to $\sim 95\%$ as we go from dark matter only simulations to full physics simulations. This large number of expected non-detections implies that in order to constrain CDM or probe the lower limit on galaxy formation by detecting dark subhalos, we may need hundreds of lensing systems as well as predictions that include the effects of central galaxies.

We note that this is not the first time that a difference between dark matter only and baryon physics simulations has been pointed out at the mass scales relevant for subhalo lensing. Despali & Vegetti (2016) used the EAGLE simulation and the Illustris full hydrodynamics run to show a similar offset. This effect appears to continue to the present day with mostly the same offset as shown by Chua et al. (2016). Additionally, several results on the scale the Milky Way show a similar offset between simulations with and without galaxy formation included (Wetzel et al., 2016; Zhu et al., 2016; Sawala et al., 2016a; Garrison-Kimmel et al.,

2017). All of these works see subhalo destruction when comparing baryonic and dark matter only simulations at the factor of two level within the virial radius. The main driver of this effect at the Milky Way scale appears to be an additional tidal field introduced by adding a physical galaxy to the system. Indeed, the effect can be reproduced by simply adding in the potential of a galaxy to a dark matter only simulation (Garrison-Kimmel et al., 2017).

As we move towards an era where we expect many more strong lensing systems suitable for substructure searches, we will need to take into account potential biases in lensing probability. One important potential bias lies within the way that subhalo mass is measured in observations. As discussed in Minor et al. (2016), the profiles used in subhalo lensing analyses could lead to underestimates in mass. This would potentially increase the measured substructure mass fractions. In addition to this observational bias there are potential biases in the simulations themselves. First, how subhalos are assigned mass by halo finders which can modify subhalo masses by a factor of 2 (see Appendix A for more details). This would similarly raise the mass fractions compared to what is seen in this work. Finally, if lens systems are biased to be viewed along a dense projection, we find that this can reduce the number of non-detections from ∼85-95% in the case of random projections to ∼60-85% in the case of looking along the most dense axis of a halo (depending on the projected radius). It is important to note that while the number of suitable lenses for substructure explorations is rather small today, we expect the number to explode in the near future owing to large-area, deep surveys such as DES, LSST, and Euclid. Simultaneously, our ability to detect substructure will substantially improve as more studies are done with ALMA, and in the near future with JWST. We expect the ability of substructure lensing to discriminate between dark matter theories will dramatically increase in the near future from two complementary approaches.

Chapter 4

Star formation history gradients as a test of supernova feedback strength

4.1 Introduction

One of the key questions that galaxy formation seeks to answer is: "How did stellar mass build up in galaxies over time?". For this reason, one important development has been using Color-Magnitude Diagrams (CMDs) along with complex stellar population synthesis models, in order to derive star formation histories for parts of a galaxy (Dolphin, 2002; Tolstoy et al., 2009; Monelli et al., 2010; Walmswell et al., 2013; Cole et al., 2014; Weisz et al., 2014a; Monelli et al., 2016; Makarova et al., 2017; Skillman et al., 2017). This is particularly useful for studying the evolution of dwarf galaxies as they can be seen in resolved stars out to around 1 Mpc with telescopes like HST, and ground-based 10m telescopes. In particular, we can gather a large statistical sample of SFHs for dwarf galaxies and begin place broad constraints on fundamental processes in the universe. For example, the SFHs of ultrafaint dwarfs appear to be almost universally old (Brown et al., 2014). This supports the idea that

these objects had their star formation quenched by reionization, leading to their universally old ages (Bullock et al., 2000; Ricotti & Gnedin, 2005). Alternatively, larger dwarf galaxies appear to be quenched preferentially within the virial radius of the Milky Way and M31, and using the fraction of quenched galaxies throughout the Local Volume we can place constraints on models of quenching (Weisz et al., 2015; Wetzel et al., 2015a; Fillingham et al., 2015). Furthermore, accurate measurements of star formation histories allow us to extrapolate galaxy properties back in time and place constraints on high-redshift luminosity and stellar mass functions (Weisz et al., 2014b; Graus et al., 2016).

A further application of the star formation histories of Local Group dwarfs is that they can be used as references to compare to hydrodynamics simulations. Comparisons between observations and simulations in the Local Group have already suggested that a deep understanding of star formation and feedback is necessary to understanding galaxy formation at small scales (Di Cintio et al., 2014; Oñorbe et al., 2015; Dutton et al., 2016; Sawala et al., 2016c; Read et al., 2016; Fitts et al., 2017).

Strong stellar feedback not only regulates the star formation, it also can change other fundamental properties of the galaxy. For example, feedback from supernovae can create cores in the dark matter halo profiles of dwarf galaxies (Pontzen & Governato, 2012; Di Cintio et al., 2014; Dutton et al., 2016; Oñorbe et al., 2015; Fitts et al., 2017). This is important as it could be a key component in solving small-scale problems with ΛCDM. For example, the cusp-core problem (Flores & Primack, 1994; Moore, 1994), where observational dwarf galaxies appear to have cored dark matter density profiles, in contrast to dark matter only simulations in which halos have NFW cusps. This can also help alleviate the "Too Big To Fail" problem (Boylan-Kolchin et al., 2011), where the larges halos in ΛCDM are too dense to host the largest galaxies seen observationally.

Similar to dark matter, the stars are also collisionless, meaning that it is possible that they are affected by strong stellar feedback as well. Such an effect was investigated by El-Badry

et al. (2016), who found that simulated dwarf galaxies with strong stellar feedback show enormous fluctuations in their effective radii over time. This effect can eventually lead to an overall median age gradient where young stars form in the center of the galaxy, and old stars are preferentially found in the outskirts. This appears to agree well with what is seen in observed dwarf galaxies, which in terms of metallicity show almost universal metallicity gradients where more metal-rich stars lie in the center and metal-poor stars in the outskirts.

Such gradients could potentially cause issues for the interpretation of CMD-derived star formation histories of dwarf galaxies, because many have only been partially covered. If age gradients are strong this could lead to a scenario where the measured star formation histories are biased in a non-trivial way from the correct answer. To that end, we investigate whether or not dwarf galaxies in the Local Group show strong variations in their star formation histories as a function of radius.

To do this we use a sample of dwarf galaxy simulations run with the GIZMO code Hopkins (2015) and the FIRE-2 feedback implementation (Hopkins et al., 2017). The format of the paper is as follows. In section 2 we will discuss the simulations that were used in this work. We will also discuss our methodology for searching for variations in star formation histories. In section 3 we will discuss how star formation histories vary with radius, and we will also discuss how sensitive this is to age gradients in the galaxy. In section 4 we then discuss the origins of these variations. Finally, in section 5 we discuss what this implies for future observations of Local Group Dwarf galaxies.

4.2 Simulations and methods

For the theoretical galaxies sample we use the dwarf galaxies introduced in Fitts et al. (2017) along with an additional suite of isolated dwarf galaxies presented for the first time

here. These dwarf galaxies were all run with the multi-method gravity+hydrodynamics code GIZMO (Hopkins, 2015). Specifically utilizing the the FIRE-2 feedback implementation (Hopkins et al., 2017). The FIRE-2 method uses a mesh-free Lagrangian Godunov (MFM) method that is second-order accurate and maintains many of the advantages of traditional SPH codes, while avoiding some of the traditional pitfalls of classic SPH codes such as accurate capturing of shocks, and general treatment of fluids, for which grid-based codes have traditionally been better at. The simulations include cooling and heating from an ionizing background, and stellar sources including stellar feedback from OB stars and AGB mass-loss, type Ia and type II supernovae, and photo-heating and radiation pressure, the inputs for which are taken directly from stellar evolution models.

The simulations themselves cover two main regimes. The Fitts et al. (2017) sample focused on the threshold of star formation by simulating 15 galaxies with halo masses of $\sim 10^{10}$ $M_{\odot}$. These simulations were run at high resolution with dark matter particle masses of $m_{dm} =$ 2500 $M_{\odot}$, and gas particle masses of $m_{gas} = 500$ $M_{\odot}$. These galaxies form between 10^5 and 10^7 $M_{\odot}$ in stellar mass in broad agreement with predictions from abundance matching. It appears as though the amount of stars that the halos form is dependent on the maximum circular velocity (V_{max}) of the host halos. This seems in agreement with the idea that galaxies with larger V_{max} formed earlier at fixed halo mass.

The focus of the second set of simulations is to fill in the gap between these isolated dwarf galaxies near the limits of galaxy formation, and galaxies at larger sizes such as the Latte simulations (Wetzel et al., 2016). The simulations in these suite were run at a resolution of $m_{dm} =$ 2.0e4 $M_{\odot}$, and gas particle masses of $m_{gas} = 4000$ $M_{\odot}$. These galaxies lie at halo masses between 2×10^{10} and 10^{11} $M_{\odot}$, forming galaxies of stellar masses between 10^7 and 10^9 $M_{\odot}$. The dwarf galaxies appear to reproduce the diversity of star formation histories seen in measurements of dwarf galaxy star formation histories (Weisz et al., 2014a). An abundance matching relation for the galaxies used in this work is shown in Fig 4.1

In order to get a sense of how the SFH should vary with radius we look at the star particle data in several different ways. The primary method of investigation involves binning the star particles as a function of radius. We restrict ourselves to 1.5 times the half-mass radius in order to study the full extent of each galaxy. In order avoid biases created by differing number of particles we divide the particles within the half-mass radius such that there is an even number of particles in each bin. We use ten bins by default, however we note that the results do not vary significantly with bin size. We further restrict ourselves so that the galaxies have $\geq$ 80 star particles per bin, or 800 star particles within 1.5 $\times$ $r_{1/2}$. We will use several different conventions when referring to radii in this work with r referring to 3D radius and R referring to projected 2D radius. Furthermore, we will often refer to three specific radii, $r_{1/2}$ the 3D half mass radius of the galaxy, $R_{1/2}$ the projected 2D half mass radius, and r_{gal} the galaxy radius, for which we follow the convention of Fitts et al. (2017) where r_{gal} is defined as 10% of the halo's virial radius.

All of these simulations are zooms The Initial conditions for all the simulations were generated using the MUSIC initial conditions generator (Hahn & Abel, 2011). Halo finding in the simulation was done using a combination of the Rockstar halo finder (Behroozi et al., 2013a), and the Amiga Halo Finder (Knollmann & Knebe, 2009, AHF). One final note is that the two sets of simulations have slightly different cosmologies with the Fitts et al. (2017) sample $H_0 = 71.0$, $\Omega_0 = 0.266$, $\Omega_b = 0.044$, $\Omega_L = 0.734$, while the new sample of large galaxies the cosmological parameters are $H_0 = 70.2$, $\Omega_0 = 0.272$, $\Omega_b = 0.0455$, $\Omega_L = 0.728$

Table 4.1: Table of properties of the galaxies used in this work. Column 1 gives the stellar mass within 10% R_{vir}, Column 2 is the halo virial mass, V_{max} is the maximum circular velocity of the halo, and R_{half} is the stellar half mass radius.

	M_{star} $[M_\odot]$	M_{halo} $[M_\odot]$	V_{max} [kms^{-1}]	R_{half} [kpc]
Halo	(1)	(2)	(3)	(4)
10+a	3.61e+06	8.88e+09	34.13	4.41
10+b	3.64e+06	1.36e+10	35.74	1.31
10+c	8.46e+06	8.52e+09	35.03	1.95
10+d	1.28e+07	1.12e+10	38.15	2.20
10+e	1.44e+07	2.40e+10	38.52	2.13
10+f	1.84e+07	1.04e+10	34.43	4.21
10+g	1.88e+07	1.53e+10	40.31	2.40
10+h	3.29e+07	2.22e+10	42.78	2.52
10+i	4.97e+07	1.47e+10	38.80	3.99
10+j	6.81e+07	3.86e+10	53.51	6.19
10+k	7.64e+07	1.87e+10	45.26	3.71
10+l	1.19e+08	3.22e+10	48.31	3.69
10+m	1.28e+08	5.21e+10	58.47	3.85
10+n	3.26e+08	4.57e+10	56.17	5.12
10+o	4.48e+08	7.58e+10	64.35	7.28
10+p	4.61e+08	6.20e+10	65.75	4.58
10+q	5.4e+08	7.44e+10	68.10	7.92
Fitts et al. (2017)				
m10b	4.65e+05	9.29e+09	31.51	0.35
m10c	5.75e+05	8.92e+09	31.40	0.36
m10e	1.98e+06	1.02e+10	31.44	0.65
m10f	4.11e+06	8.56e+09	35.66	0.80
m10h	7.80e+06	1.28e+10	37.98	0.88
m10j	9.74e+06	1.10e+10	37.98	0.72
m10k	1.04e+07	1.15e+10	38.22	1.19
m10l	1.30e+07	1.06e+10	37.62	0.81
m10m	1.44e+07	1.15e+10	38.51	1.00

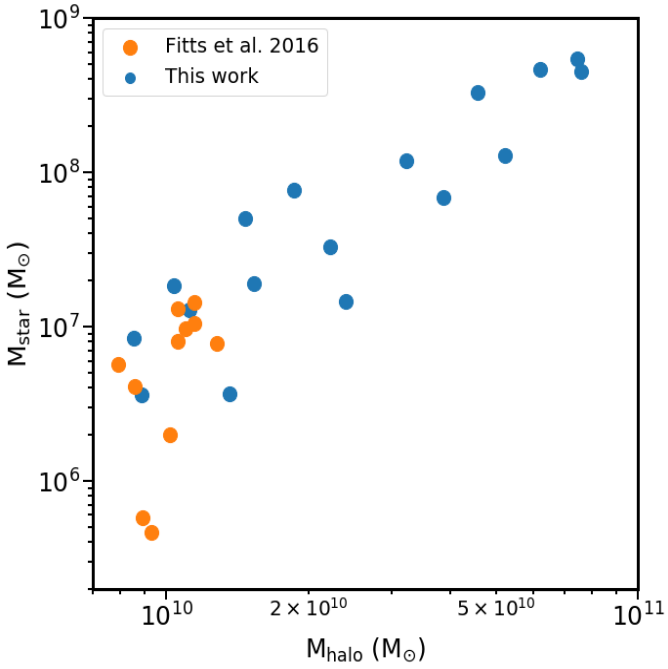

Figure 4.1: Stellar mass vs. halo mass for simulated galaxies used in this work.

4.3 Discussion

4.3.1 Star formation history gradients

Figure 4.2 shows examples of the star formation history gradients for three galaxies throughout the sample. The left panel shows a schematic diagram of the bins in radius colored by the median age of stars in the bin, and the right side shows the SFHs in each bin colored by their distance from the center in terms of the projected half mass radius (along the z-axis). The stellar mass of the galaxies is shown in the top-left corner. It can clearly be seen that most of the isolated dwarf galaxies in FIRE-2 show radial gradients to some extent, moving in the same direction, with younger stars in the center and older stars in the outskirts. Similar maps for all galaxies in the sample are shown in the appendix.

We also present the star formation history gradients in two alternative ways by defining two parameters: the time it takes a star formation history to reach 50% of its final mass (t_{50}) and

the time it takes a star formation history to reach 90% of its final mass (t_{90}). We measure t_{50} and t_{90} in each of the bins for every galaxy in the sample. This allows us to plot the gradients as a function of radius.

Examples of this are shown in Figure 4.3, for the same galaxies as in Figure 4.2. Gradients for all of the galaxies looked at in the sample are shown in the appendix. One important difference to note is that Figure 4.3 is in projection, where as Figure 4.2 is binned in 3D. In order to account for differences in the gradient with projection we averaged the gradient over 100 different projections through each galaxy, with the full extent shown as a shaded region. Representing the gradients in terms of t_{50} and t_{90} as a function of radius allows us to show how these gradients should vary with radius. Regardless, of the parameter used, the galaxy we look at, and the projection through that galaxy, all but one of the dwarf galaxies in the sample show negative age gradients, where the stars are younger in the inner regions, and older in the outskirts, some gradients are small, and consistent with flat with in the scatter given by project, but most are clearly negative.

In order to look for trends of these gradients with various parameters, we further measure the slopes of the t_{50} and t_{90} age gradients which we define as:

$$\gamma_{50} = \frac{\Delta t_{50}}{\Delta r}; \gamma_{90} = \frac{\Delta t_{90}}{\Delta r}$$

We measure the slope of the gradient in two different ways. First, we take the difference between t_{50} and t_{90} in the inner and outer bins, and then divide it by the difference in the mean radius of the inner and outer bins. To double check this, we also measure the slope by calculating the least squares fit to a line, and taking the slope of that line. The different methods of measuring the slope make little difference in the actual measured slope, so we

do not consider it further.

Now we want to look for trends in this parameter in order to give some hint as to their origin. One intriguing relation that can be seen in Figure 4.4 is that between the slope of the gradient, and the total t_{50} or t_{90} of the galaxy. In general, the isolated dwarf galaxies in FIRE-2 show wider (more negative) age gradients for older galaxies, and smaller (less negative) gradients when the galaxy is later forming. In the next section we look into the origin of this relation

4.3.2 Origin of the age gradients

The physical origin of the SFH gradients and their trend with formation time could be due to several processes. In principle, any physical process which dynamically heats stellar distributions could be responsible for driving this age gradient. Of key importance to understanding the physical origin of the gradients lies in explaining the trend with formation time. In this work we look at two potential processes which could be responsible, the first is galaxy mergers.

Both galaxy mergers and mergers with dark matter halos containing no stars could drive the SFH gradients. Mergers with dark matter halos can dynamically heat the stellar distributions Starkenburg & Helmi (2015); Benítez-Llambay et al. (2016); Leaman et al. (2017). Since these mergers tend to happen at early times they, in principle, could be responsible for driving the spread with formation time as they would be more likely to heat older stars. Furthermore, galaxy mergers could drive age gradients both by dynamical heating, and by adding stars to the outskirts of the galaxy, similar to how the stellar halo of Milky Way size galaxies is believed to be built Bullock & Johnston (2005b); Cooper et al. (2010). Furthermore, mergers with galaxies at this mass scale would most likely include many ultrafaint dwarf galaxies with very old stellar populations, which could also potentially explain the trend with formation

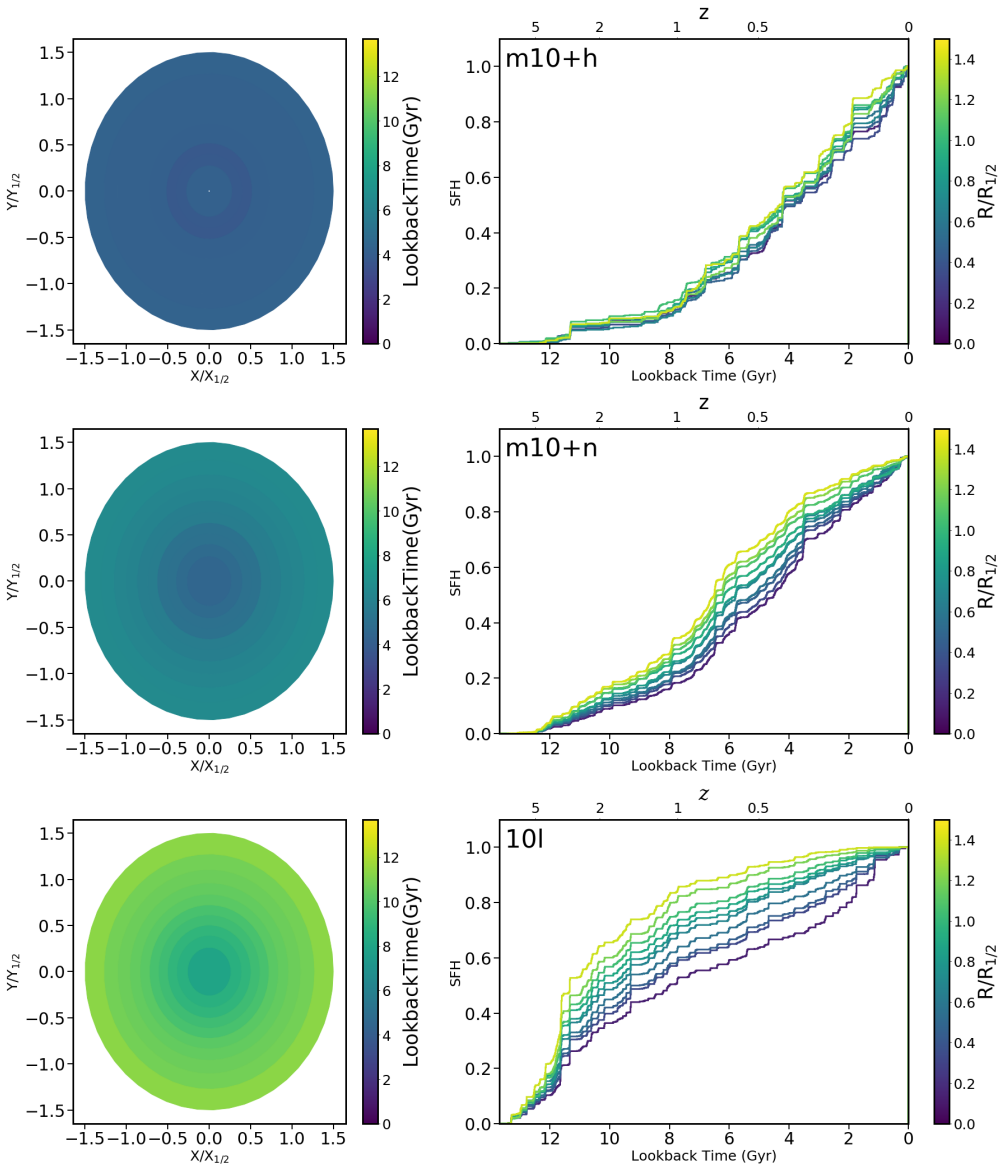

Figure 4.2: Examples of SFHs for isolated dwarf galaxies in FIRE. *Left:* is a map of the galaxy in shells around the center colored by the median age of the stars within that bin. *Right:* The star formation history within each bin, now colored by the distance of the bin from the center of the galaxy. The galaxies presented are chosen to be representative of the full width of gradients from the simulations with one weak, intermediate, and strong gradient shown. Note that regardless of the strength of the gradient the inner regions of the galaxy are later forming than the inner regions. Maps for all of the galaxies used in this work are presented in the appendix.

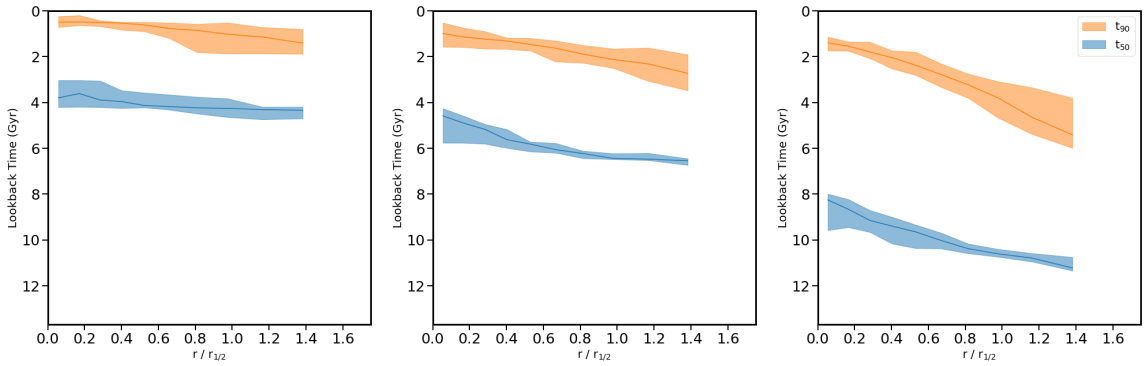

Figure 4.3: Gradients for the same galaxies as in Figure 4.2 but represented in an alternative way, by measuring t_{50} (blue) and t_{90} (orange) in each bin and presenting them as a function of radius. This is done in projection with the shaded region showing the total spread for 100 different projections through the galaxy. The solid line represents the median of the gradient over all 100 projections. The dashed and dot-dashed lines represent two different methods of measuring the slopes: using a least squares fit to the data, and simply calculating the difference in the first and last bins.

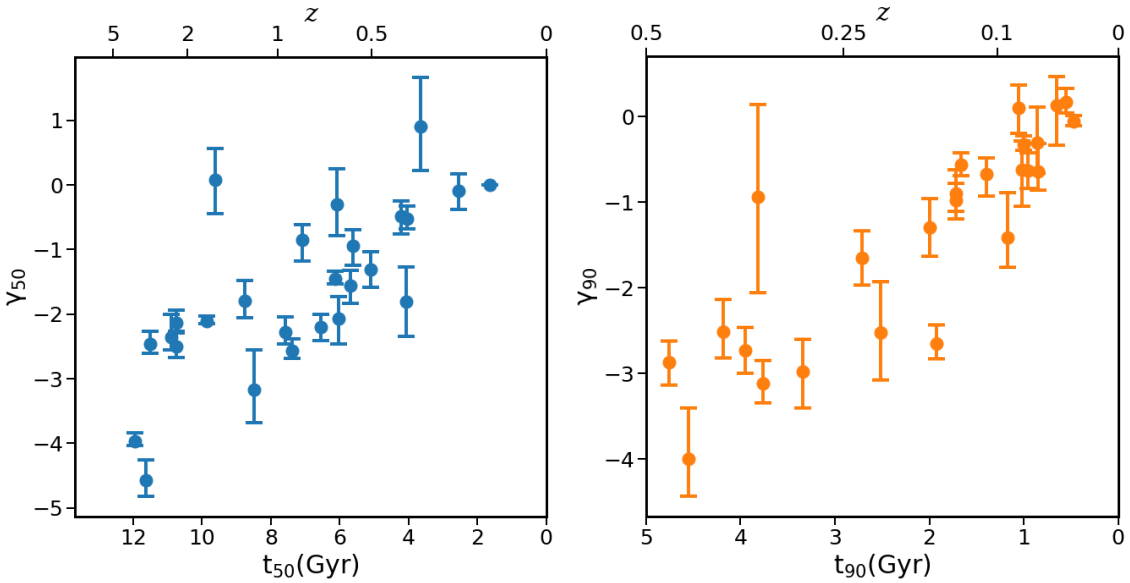

Figure 4.4: slopes of the SFH gradients for all of the galaxies in the sample, plotted against the t_{50} (left) or t_{90} (right) of the total SFH for the galaxy. There is a very clear trend with star formation time, such that galaxies that form earlier tend to have stronger gradients.

time.

However, we believe this scenario is not a dominant cause of the stellar age gradients for a few reasons. First, of all, these galaxies do not have very many galaxy-galaxy mergers. Fitts et al. (2018) studied the merger histories of the galaxies from Fitts et al. (2017) which are also included in this sample, and found that in most of these galaxies $\leq 10\%$ of their stars are accreted. Only two of the Fitts et al. (2017) sample accreted more than 10% of their stars. These galaxies (m10q and m10f) show very strong age gradients relative to the other galaxies from the Fitts et al. (2017) sample. Furthermore, while these galaxies do tend to have more mergers with completely dark halos, they tend to be at very high redshift ($z > 5$) implying that if dynamical heating due to dark matter halos were responsible there would be even stronger age gradients as there would be no way to heat more recently formed stars.

The second mechanism that could be responsible for driving the age gradients in these galaxies is stellar feedback. There are two mechanisms related to stellar feedback that could drive the SFH gradients. First, is the gradual heating of stars due to changes in the galaxy potential from stellar feedback. Such a mechanism is believed to be responsible for the creation of cores in dark matter halos. Because the star particles are collision-less similar to dark matter particles in the simulations, it is reasonable that they could be impacted by feedback in a similar way. The second mechanism is stars formed out of feedback events, which blow out gas, compressing it, and triggering star formation. Such star formation event have been seen observationally, both near supernova remnants, and in galactic outflows.

Theoretically, El-Badry et al. (2016) looked at the impact of stellar feedback on the stellar distributions within FIRE-2 galaxies at a range of stellar masses and found that while both of these types of stellar feedback impact the stellar distributions. However, the second effect of stars forming out of feedback events triggering star formation is the primary driver of creating age gradients. Furthermore, this scenario helps explain the relation between the strength of the SFH gradient and the formation time of the galaxy, as older stellar distributions will have

had more time to be modified by feedback. Additionally, because feedback events continue happening throughout the entire history of the galaxy this allows for more recently forming stars to be found in the outer parts of the galaxy.

4.4 Comparison to observed dwarf galaxies

In general, it has long been known that the classical dwarf satellites of the Milky Way and galaxies throughout the Local Volume show age metallicity gradients (Harbeck et al., 2001; Battaglia et al., 2006; Bernard et al., 2008; McConnachie, 2012; Martínez-Vázquez et al., 2015; Okamoto et al., 2017; Kacharov et al., 2017). These age and metallicity gradients appear to be in the same direction of those in simulated galaxies presented in this work. With younger, metal-rich stars found in the central regions, and older, metal-poor stars further out. However, to date, observations of the distribution of stellar ages as a function of radius, are rare, particularly at this mass-scale making a direct comparison difficult.

One of the closer comparisons we can make is to the data presented in Hidalgo et al. (2013), who observed four nearby dwarf galaxies (Cetus, Tucana, LGS3, and Phoenix), and measured the star formation history of these galaxies in radial bins. The results once again qualitatively agree, with LGS-3 and Phoenix showing a fairly strong spread in SFH where the age of the last forming star increases with increasing radius. Tucana shows a smaller spread in its star formation history, and Cetus has no detectable spread. It is difficult to use this data to quantify whether or not the formation time is correlated to the spread in the SFH. If anything, the real galaxies from Hidalgo et al. (2013) show the opposite trend, with the galaxies with smaller gradients (Cetus and Tucana) being older, however both of these galaxies are quenched whereas all the isolated dwarf galaxies in FIRE studied in this paper are actively star forming.

Another comparison that can be made is to various IFU surveys of galaxies that have become common over the past several years. Because these surveys return numerous spectra throughout the entire field of view of the telescope it make it possible to measure the SFH within every pixel of the galaxy observed. Such surveys have been used to measure spatially resolved star formation histories such as (Garcia-Benito+17), who measured the spatially resolved star formation histories for 661 galaxies within the CALIFA survey. The stellar mass range of their targeted galaxies is $10^{8.4}$ to 10^{12} $M_{\odot}$, and thus only the most massive of the galaxies in our sample are directly comparable to the results from the CALIFA survey. However, there are some interesting trends that are hinted at in this work. In general, they find their galaxies show age gradients with older stars in the central regions, and younger stars at the outskirts consistent with spiral galaxies containing bulges, and elliptical galaxies evolving from spirals. These massive galaxies also show very weak gradients in their SFHs. Interestingly, this gradient actually strengthens in the smallest bin in their sample $M_{star} = 10^{8.4}$ to $10^{9.9}$. In this bin, the stars are in general later forming, but the gradient between the inner and outermost regions is larger. This could potentially point toward some interesting evolution between the largest galaxies in our sample which show very small negative age gradients, and the smallest galaxies in the CALIFA sample which show large positive age gradients. However, in order to decouple these issue more observations of spatially resolved star formation histories for small galaxies are needed.

4.5 Impact on future star formation history measurement

If dwarf galaxies show strong star formation history gradients as seen in this work it could impact the interpretation of current measurements of star formation histories, and plans of future measurements. This is because CMD-derived star formation histories often rely on

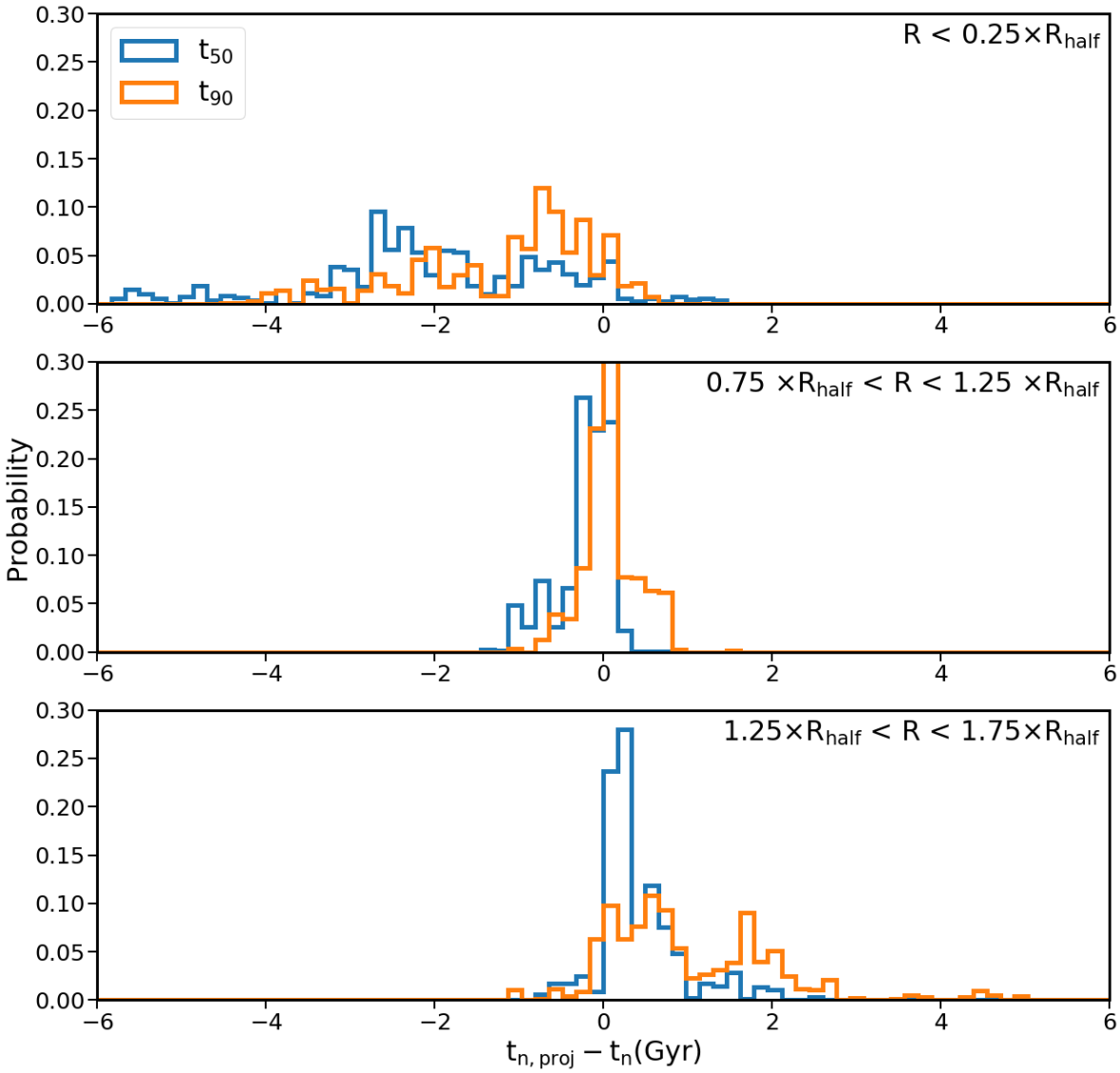

Figure 4.5: The total spread in measured t_{50} (blue) and t_{90} (orange) for all the galaxies in this sample. The value is measured relative to t_{50} or t_{90} for the total of the stellar distribution within r_{gal} (10% of the virial radius of the galaxy's dark matter halo in 3D). The figure is divided into three regions throughout the galaxy, one in the inner regions of the galaxy ($0.25\times R_{half}$), at R_{half}, and in the outskirts of the galaxy ($1.5\times R_{half}$). The histograms represent the error in derived SFH over all the galaxies in the sample and for 100 projections through each galaxy.

telescopes such as HST which for nearby galaxies may only cover 10% or less of the galaxy. If the galaxy has a strong age gradient it can lead to large discrepancies in the star formation history from incomplete coverage. One can estimate the potential pitfalls by looking at the spread in SFHs as a function of radius. Obviously, the uncertainty in SFH depends on several factors including the distance from the center of the galaxy, the size of the field of view used to calculate the SFH, and the steepness of the gradient. Observationally, the first two are known, but the strength of the gradient cannot be determined observationally without measuring the SFH. Rough estimates of this effect can be estimated through the use of theoretical studies such as this.

We attempt to estimate the potential range of error in SFH history based off of our simulation suite in figure 4.5. First we compute value t_{50} or t_{90} measured across all the galaxies in the sample in projection over 100 different projections through the halo. The figure shows the error in this data relative to the true value of t_{50} or t_{90} for all the stars within r_{gal} defined as 10% of the virial radius of the galaxy's dark matter halo. In order to get a sense of how this varies with radius we do this same procedure in three different bins within $0.25\times R_{half}$, at R_{half}, and at $1.5\times R_{half}$. The bias in the SFH measured at different points throughout the galaxy works in the direction one would expect, the inner regions of the galaxy are biased younger than the true value, and the outskirts are biased older than the true value. Interestingly, the SFH measured around the half mass radius matches quite well to the true value, with a relatively small scatter.

This result has important implications for the future of measuring ages of stars using only parts of the galaxy. Without a careful accounting for the age gradient significant errors in the SFH can result. Where fields should be placed within galaxies in order to recover the correct star formation history will become even more important in the future for JWST which has a similar field of view as HST, but will be able to measure star formation histories for many more galaxies throughout the Local Volume. Even further on the in the future

WFIRST will be able to cover most of the area of galaxies throughout the Local Volume, however crowding effects could limit the ability to get accurate star formation histories for the inner regions of these galaxies, implying such star formation histories will be biased older than the total stellar distribution.

4.6 Conclusion

In this work we have noted the presence of star formation history gradients in dwarf galaxies within FIRE-2. For galaxies with stellar masses of $10^{5.5}$ to $10^{8.6}$ $M_{\odot}$, galaxies almost universally show gradients in their star formation histories with younger stars at the center and older stars at the outskirts. The slope of the gradients varies widely between galaxies, and does not seem to show a strong correlation with stellar mass and halo mass. However, there does seem to be a strong correlation between the slope of the age gradient and formation time of the galaxy.

The origin of these age gradients is feedback from stars which launches strong outflows which subsequently form stars. Older galaxies have stronger gradients primarily because the strength of feedback is more pronounced on early forming galaxies of a similar halo mass. This is because more of the galaxy's mass was assembled when the halo was smaller, allowing gas to be launched further before forming stars. These earlier forming galaxies have also had a longer time for their stars to be dynamically heated by multiple feedback episodes changing the gravitational potential of the galaxy via the removal of gas.

Observational comparisons to available data are difficult, however there are some broad consistencies. First, dwarf galaxies are well known to have median age gradients with younger stars at the center and older stars at the outskirts. Furthermore, resolved star formation history work such as that in Hidalgo et al. (2013) has focused on the variation of star

formation history with radius that seems to support the existence of star formation history gradients, but provides weak evidence of a trend with formation time.

The observation of SFH gradients in dwarf galaxies has several implications for the future of galaxy formation studies. If dwarf galaxies in the Local Volume show a gradient in their SFHs, measuring how this gradient scales with formation time could be useful in calibrating feedback models. However, accurate calibration of feedback models would require resolved SFHs for many dwarf galaxies at several radii in order to accurately measure the slopes of the gradient.

One other important implication is the spread in star formation history is large enough that star formation histories derived from single field CMDs may not be accurate. The SFH can vary wildly with radius, potentially biasing results from small fields by a few Gyrs. Thus truly understanding the formation of dwarf galaxies will require observations covering large areas of the galaxy, or at least some correction for how incomplete coverage can bias measurements of the star formation history. Such considerations must be taken into account in the era of telescopes such as JWST, WFIRST and 30m-class telescopes.

Bibliography

Alvarez M. A., Finlator K., Trenti M., 2012, ApJl, 759, L38

Baldry I. K., et al., 2012, MNRAS, 421, 621

Battaglia G., et al., 2006, AAP, 459, 423

Behroozi P. S., Wechsler R. H., Wu H.-Y., 2013a, ApJ, 762, 109

Behroozi P. S., Wechsler R. H., Wu H.-Y., Busha M. T., Klypin A. A., Primack J. R., 2013b, ApJ, 763, 18

Benítez-Llambay A., Navarro J. F., Abadi M. G., Gottlöber S., Yepes G., Hoffman Y., Steinmetz M., 2016, MNRAS, 456, 1185

Bernard E. J., et al., 2008, ApJl, 678, L21

Bolton A. S., Treu T., Koopmans L. V. E., Gavazzi R., Moustakas L. A., Burles S., Schlegel D. J., Wayth R., 2008, ApJ, 684, 248

Bourassa R. R., Kantowski R., Norton T. D., 1973, ApJ, 185, 747

Bouwens R. J., Illingworth G. D., Oesch P. A., Caruana J., Holwerda B., Smit R., Wilkins S., 2015, ApJ, 811, 140

Bovill M. S., Ricotti M., 2009, ApJ, 693, 1859

Bovy J., Erkal D., Sanders J. L., 2016, preprint, (`arXiv:1606.03470`)

Boylan-Kolchin M., Bullock J. S., Kaplinghat M., 2011, MNRAS, 415, L40

Boylan-Kolchin M., Bullock J. S., Kaplinghat M., 2012, MNRAS, 422, 1203

Boylan-Kolchin M., Bullock J. S., Sohn S. T., Besla G., van der Marel R. P., 2013, ApJ, 768, 140

Boylan-Kolchin M., Bullock J. S., Garrison-Kimmel S., 2014, MNRAS, 443, L44

Boylan-Kolchin M., Weisz D. R., Johnson B. D., Bullock J. S., Conroy C., Fitts A., 2015, MNRAS, 453, 1503

Brooks A. M., Zolotov A., 2014, ApJ, 786, 87

Brooks A. M., Kuhlen M., Zolotov A., Hooper D., 2013, ApJ, 765, 22

Brown T. M., et al., 2014, ApJ, 796, 91

Bullock J. S., Boylan-Kolchin M., 2017, araa, 55, 343

Bullock J. S., Johnston K. V., 2005a, ApJ, 635, 931

Bullock J. S., Johnston K. V., 2005b, ApJ, 635, 931

Bullock J. S., Kravtsov A. V., Weinberg D. H., 2000, ApJ, 539, 517

Carlberg R. G., 2009, ApJl, 705, L223

Chua K. T. E., Pillepich A., Rodriguez-Gomez V., Vogelsberger M., Bird S., Hernquist L., 2016, preprint, (arXiv:1611.07991)

Cole A. A., Weisz D. R., Dolphin A. E., Skillman E. D., McConnachie A. W., Brooks A. M., Leaman R., 2014, ApJ, 795, 54

Collett T. E., 2015, ApJ, 811, 20

Cooper A. P., et al., 2010, MNRAS, 406, 744

D'Onghia E., Springel V., Hernquist L., Keres D., 2010, ApJ, 709, 1138

Dalal N., Kochanek C. S., 2002, ApJ, 572, 25

Despali G., Vegetti S., 2016, preprint, (arXiv:1608.06938)

Despali G., Vegetti S., White S. D. M., Giocoli C., van den Bosch F. C., 2017, preprint, (arXiv:1710.05029)

Di Cintio A., Brook C. B., Macciò A. V., Stinson G. S., Knebe A., Dutton A. A., Wadsley J., 2014, MNRAS, 437, 415

Dolphin A. E., 2002, MNRAS, 332, 91

Duncan K., et al., 2014, MNRAS, 444, 2960

Dutton A. A., Macciò A. V., Frings J., Wang L., Stinson G. S., Penzo C., Kang X., 2016, MNRAS, 457, L74

Efstathiou G., 1992a, MNRAS, 256, 43P

Efstathiou G., 1992b, MNRAS, 256, 43P

El-Badry K., Wetzel A., Geha M., Hopkins P. F., Kereš D., Chan T. K., Faucher-Giguère C.-A., 2016, ApJ, 820, 131

Elbert O. D., Bullock J. S., Garrison-Kimmel S., Rocha M., Oñorbe J., Peter A. H. G., 2015, MNRAS, 453, 29

Fiacconi D., Madau P., Potter D., Stadel J., 2016, ApJ, 824, 144

Fillingham S. P., Cooper M. C., Wheeler C., Garrison-Kimmel S., Boylan-Kolchin M., Bullock J. S., 2015, MNRAS, 454, 2039

Fitts A., et al., 2017, MNRAS, 471, 3547

Fitts A., et al., 2018, preprint, (arXiv:1801.06187)

Flores R. A., Primack J. R., 1994, ApJl, 427, L1

Furlong M., et al., 2015, MNRAS, 450, 4486

Garrison-Kimmel S., Boylan-Kolchin M., Bullock J. S., Lee K., 2014, MNRAS, 438, 2578

Garrison-Kimmel S., et al., 2017, preprint, (arXiv:1701.03792)

Genel S., et al., 2014, MNRAS, 445, 175

Gilman D., Agnello A., Treu T., Keeton C. R., Nierenberg A. M., 2017, MNRAS,

Gnedin N. Y., Kravtsov A. V., 2006, ApJ, 645, 1054

González V., Labbé I., Bouwens R. J., Illingworth G., Franx M., Kriek M., 2011, ApJl, 735, L34

Graus A. S., Bullock J. S., Boylan-Kolchin M., Weisz D. R., 2016, MNRAS, 456, 477

Grazian A., et al., 2015, AAP, 575, A96

Green A. M., Hofmann S., Schwarz D. J., 2004, MNRAS, 353, L23

Hahn O., Abel T., 2011, MNRAS, 415, 2101

Harbeck D., et al., 2001, AJ, 122, 3092

He Q., Li R., Lim S., Frenk C. S., Cole S., Peng E. W., Wang Q., 2017, preprint, (arXiv:1707.01849)

Hezaveh Y. D., et al., 2016, ApJ, 823, 37

Hidalgo S. L., et al., 2013, ApJ, 778, 103

Hopkins P. F., 2015, MNRAS, 450, 53

Hopkins P. F., et al., 2017, preprint, (arXiv:1702.06148)

Hsueh J.-W., Despali G., Vegetti S., Xu D., Fassnacht C. D., Metcalf R. B., 2017a, preprint, (arXiv:1707.07680)

Hsueh J.-W., et al., 2017b, MNRAS, 469, 3713

Ibata R. A., Lewis G. F., Irwin M. J., Quinn T., 2002, MNRAS, 332, 915

Ilbert O., et al., 2013, AAP, 556, A55

Jaacks J., Thompson R., Nagamine K., 2013, ApJ, 766, 94

Jiang F., van den Bosch F. C., 2017, MNRAS, 472, 657

Johnston K. V., Spergel D. N., Haydn C., 2002, ApJ, 570, 656

Kacharov N., et al., 2017, MNRAS, 466, 2006

Klypin A., Kravtsov A. V., Valenzuela O., Prada F., 1999, ApJ, 522, 82

Knebe A., et al., 2011, MNRAS, 415, 2293

Knollmann S. R., Knebe A., 2009, ApJs, 182, 608

Kuhlen M., Faucher-Giguère C.-A., 2012, MNRAS, 423, 862

Kuhlen M., Diemand J., Madau P., 2008, ApJ, 686, 262

Larson D., et al., 2011, ApJs, 192, 16

Leaman R., et al., 2017, MNRAS, 472, 1879

Lowing B., Wang W., Cooper A., Kennedy R., Helly J., Cole S., Frenk C., 2015, MNRAS, 446, 2274

Lu Y., et al., 2014, ApJ, 795, 123

Lukić Z., Heitmann K., Habib S., Bashinsky S., Ricker P. M., 2007, ApJ, 671, 1160

MacLeod C. L., Jones R., Agol E., Kochanek C. S., 2013, ApJ, 773, 35

Madau P., Weisz D. R., Conroy C., 2014, ApJl, 790, L17

Makarova L. N., Makarov D. I., Karachentsev I. D., Tully R. B., Rizzi L., 2017, MNRAS, 464, 2281

Mao S., Schneider P., 1998, MNRAS, 295, 587

Marchesini D., van Dokkum P. G., Förster Schreiber N. M., Franx M., Labbé I., Wuyts S., 2009, ApJ, 701, 1765

Martínez-Vázquez C. E., et al., 2015, MNRAS, 454, 1509

Mateo M. L., 1998, araa, 36, 435

McConnachie A. W., 2012, AJ, 144, 4

Metcalf R. B., 2005, ApJ, 629, 673

Metcalf R. B., Madau P., 2001, ApJ, 563, 9

Minor Q. E., Kaplinghat M., Li N., 2016, preprint, (arXiv:1612.05250)

Monelli M., et al., 2010, ApJ, 722, 1864

Monelli M., et al., 2016, ApJ, 819, 147

Moore B., 1994, nature, 370, 629

Moore B., Ghigna S., Governato F., Lake G., Quinn T., Stadel J., Tozzi P., 1999, ApJl, 524, L19

Moustakas J., et al., 2013, ApJ, 767, 50

Murray S. G., Power C., Robotham A. S. G., 2013, Astronomy and Computing, 3, 23

Nelson D., et al., 2015, Astronomy and Computing, 13, 12

Ng K. C. Y., Laha R., Campbell S., Horiuchi S., Dasgupta B., Murase K., Beacom J. F., 2014, PRD, 89, 083001

Nierenberg A. M., Treu T., Wright S. A., Fassnacht C. D., Auger M. W., 2014, MNRAS, 442, 2434

Nierenberg A. M., et al., 2017, MNRAS, 471, 2224

Oñorbe J., Boylan-Kolchin M., Bullock J. S., Hopkins P. F., Kereš D., Faucher-Giguère C.-A., Quataert E., Murray N., 2015, MNRAS, 454, 2092

Oñorbe J., Hennawi J. F., Lukić Z., 2016, preprint, (arXiv:1607.04218)

Okamoto T., Gao L., Theuns T., 2008, MNRAS, 390, 920

Okamoto S., Arimoto N., Tolstoy E., Jablonka P., Irwin M. J., Komiyama Y., Yamada Y., Onodera M., 2017, MNRAS, 467, 208

Onions J., et al., 2012, MNRAS, 423, 1200

Pérez-González P. G., et al., 2008, ApJ, 675, 234

Planck Collaboration et al., 2016, AAP, 596, A108

Polisensky E., Ricotti M., 2011, PRD, 83, 043506

Pontzen A., Governato F., 2012, MNRAS, 421, 3464

Read J. I., Agertz O., Collins M. L. M., 2016, MNRAS, 459, 2573

Ricotti M., Gnedin N. Y., 2005, ApJ, 629, 259

Robertson B. E., Ellis R. S., Furlanetto S. R., Dunlop J. S., 2015, ApJl, 802, L19

Rocha M., Peter A. H. G., Bullock J., 2012, MNRAS, 425, 231

Sánchez-Conde M. A., Cannoni M., Zandanel F., Gómez M. E., Prada F., 2011, jcap, 12, 011

Santini P., et al., 2012, AAP, 538, A33

Sawala T., et al., 2015, MNRAS, 448, 2941

Sawala T., Pihajoki P., Johansson P. H., Frenk C. S., Navarro J. F., Oman K. A., White S. D. M., 2016a, preprint, (arXiv:1609.01718)

Sawala T., et al., 2016b, MNRAS, 456, 85

Sawala T., et al., 2016c, MNRAS, 457, 1931

Sawala T., et al., 2016d, MNRAS, 457, 1931

Schaller M., et al., 2015, MNRAS, 451, 1247

Schaye J., et al., 2015a, MNRAS, 446, 521

Schaye J., et al., 2015b, MNRAS, 446, 521

Schultz C., Oñorbe J., Abazajian K. N., Bullock J. S., 2014, MNRAS, 442, 1597

Shapiro P. R., Giroux M. L., Babul A., 1994, ApJ, 427, 25

Sheth R. K., Mo H. J., Tormen G., 2001, MNRAS, 323, 1

Skillman E. D., et al., 2017, ApJ, 837, 102

Somerville R. S., Davé R., 2015, araa, 53, 51

Song M., et al., 2016, ApJ, 825, 5

Springel V., White S. D. M., Tormen G., Kauffmann G., 2001, MNRAS, 328, 726

Springel V., Frenk C. S., White S. D. M., 2006, nature, 440, 1137

Starkenburg T. K., Helmi A., 2015, AAP, 575, A59

Taylor C., Boylan-Kolchin M., Torrey P., Vogelsberger M., Hernquist L., 2016, MNRAS, 461, 3483

Tollerud E. J., Bullock J. S., Strigari L. E., Willman B., 2008, ApJ, 688, 277

Tolstoy E., Hill V., Tosi M., 2009, araa, 47, 371

Tomczak A. R., et al., 2014, ApJ, 783, 85

Vegetti S., Koopmans L. V. E., Bolton A., Treu T., Gavazzi R., 2010, MNRAS, 408, 1969

Vegetti S., Lagattuta D. J., McKean J. P., Auger M. W., Fassnacht C. D., Koopmans L. V. E., 2012, nature, 481, 341

Vegetti S., Koopmans L. V. E., Auger M. W., Treu T., Bolton A. S., 2014, MNRAS, 442, 2017

Vogelsberger M., et al., 2014a, MNRAS, 444, 1518

Vogelsberger M., et al., 2014b, MNRAS, 444, 1518

Walmswell J. J., Eldridge J. J., Brewer B. J., Tout C. A., 2013, MNRAS, 435, 2171

Wang W., Han J., Cooper A. P., Cole S., Frenk C., Lowing B., 2015, MNRAS, 453, 377

Weisz D. R., Dolphin A. E., Skillman E. D., Holtzman J., Dalcanton J. J., Cole A. A., Neary K., 2013, MNRAS, 431, 364

Weisz D. R., Dolphin A. E., Skillman E. D., Holtzman J., Gilbert K. M., Dalcanton J. J., Williams B. F., 2014a, ApJ, 789, 147

Weisz D. R., Johnson B. D., Conroy C., 2014b, ApJl, 794, L3

Weisz D. R., Dolphin A. E., Skillman E. D., Holtzman J., Gilbert K. M., Dalcanton J. J., Williams B. F., 2015, ApJ, 804, 136

Wetzel A. R., Deason A. J., Garrison-Kimmel S., 2015a, ApJ, 807, 49

Wetzel A. R., Tollerud E. J., Weisz D. R., 2015b, ApJl, 808, L27

Wetzel A. R., Hopkins P. F., Kim J.-h., Faucher-Giguère C.-A., Kereš D., Quataert E., 2016, ApJl, 827, L23

Wheeler C., Oñorbe J., Bullock J. S., Boylan-Kolchin M., Elbert O. D., Garrison-Kimmel S., Hopkins P. F., Kereš D., 2015, MNRAS, 453, 1305

White S. D. M., Rees M. J., 1978, MNRAS, 183, 341

Wise J. H., Demchenko V. G., Halicek M. T., Norman M. L., Turk M. J., Abel T., Smith B. D., 2014, MNRAS, 442, 2560

Zhu Q., Marinacci F., Maji M., Li Y., Springel V., Hernquist L., 2016, MNRAS, 458, 1559

van der Marel R. P., Fardal M., Besla G., Beaton R. L., Sohn S. T., Anderson J., Brown T., Guhathakurta P., 2012, ApJ, 753, 8